FINAL REPORT

Project Title: Shock-Driven Hydrodynamic Instability Growth Near Phase Boundaries and Material Property Transitions

Coverage Period: August 15, 2012 through August 14, 2016

Date of Report: March, 1 2017

Recipient: Arizona State University (ASU)

Award Number: DE-SC0008683

Contact(s): Dr. Pedro Peralta, 480-965-2894, pperalta@asu.edu

Project Team: Elizabeth Fortin, PhD student, ASU, evfortin@asu.edu
Saul Opie**,** PhD student, ASU, sopie@asu.edu
Sudrishti Gautam, MS Student, ASU, sgautam1@asu.edu
Ashish Gopalakrishnan, MS student, ASU, agopala8@asu.edu
Jenna Lynch, Arizona State University, jlynch6@asu.edu
Y. Chen, undergraduate student, ASU, ychen291@asu.edu
Eric Loomis, Los Alamos National Laboratory, loomis@lanl.gov

Project Objective:

This project is concerned with developing experiments for measuring dynamic material strength changes across solid-solid phase transitions in metals to assist with the development of phase-aware strength models for numerical simulations. The fundamental idea of our experiments is to infer these changes to material strength properties by measuring Richtmyer-Meshkov (RM) growth rates (and similar instability phenomena) in metals shocked across high-pressure phase boundaries. Extrapolation of single phase behavior to multi-phase behavior is assumed. This effort has been undertaken with Los Alamos National Laboratory (LANL) personnel and testing facilities in close collaboration with ASU faculty, graduate and undergraduate students who performed sample fabrication, post-mortem sample characterization, and numerical and analytical analysis.

Background:

Characterizing the response of materials subjected to high loads and strain rates from shock loading is important to a wide variety of scientific and technical applications. In these applications shock waves often encounter material, loading, or geometry perturbations leading to large deviatoric deformations (i.e., perturbation growth) once the ideal uniaxial strain condition is violated [1]. Often these perturbations and subsequent growth are critical to performance metrics such as in inertial confinement fusion where surface perturbation seeding and growth prevents efficient ignition [2].

In many applications one or both materials can be solids with significant elastic shear strength that can appreciably alter the perturbation growth evolution from that of a strictly fluid (hydrodynamic) analysis [3,4,5]. Solids

also often possess strength anisotropy and rate dependence that can seed perturbations and affect perturbation growth, respectively [6]. A relatively unexplored material phenomenon related to hydrodynamic instabilities is the effect that phase transformations have on perturbation growth evolution. Many solids under dilatational, e.g., iron, or shear strains, e.g., shape memory alloys, undergo diffusionless "martensitic" phase transformation. In the case of iron the phase change could have significant effects on perturbation growth since low pressure iron has a body center cubic (BCC) structure while the high pressure phase is hexagonal close packed (HCP); these two structures are known to have significantly different properties [7]. In addition the existence of a phase change often changes the dynamics of the shock front and its propagation, as is the case for iron, which may lead to other effects on perturbation growth.

Another challenge for instability modeling, and high dynamic strain rates in general, is a lack of experimental data. Typical plate impact and similar shock experiments are inherently one-dimensional and provide significant but limited information for strength model validation [8]. Recently, there has been increasing interest in using Rayleigh-Taylor (RT) [9] and Richtmyer-Meshkov (RM) [10] instability experiments for material model calibration and validation. In these experiments modern dynamic diagnostic tools such as proton radiography [11] and x-ray radiography [10] have typically been used to capture the surface evolution; however, these diagnostic capabilities are beyond the reach of most research labs; therefore, experimental data is sparse [12]. Also RT experiments tend to be very sensitive to initial and boundary conditions, which can have a significant influence on perturbation growth at later stages, hence uncertainty of these initial and boundary conditions can significantly limit the confidence of parameters obtained from simulations utilizing RT experiments. The experiments developed in this project compliment RT and RM experiments, providing additional validation data without some of the drawbacks found in RT experiments.

Status: Activities for this grant included: 1) Development of dynamic impact experiments to probe strength and phase transition influence on dynamic deformation, 2) development of modern strength and phase aware simulation capabilities, 3) and post-processing of experimental data with simulation and closed form analytical techniques.

Two different dynamic experiments were developed to probe material strengths in solid metals (largely copper and iron in this effort). In the first experiment a flyer plate impacts a flat target with an opposite rippled surface that is partially supported by a weaker window material. Post mortem analysis of the target sample showed a strong and repeatable residual plastic deformation dependence on grain orientation [13]. Yield strengths for strain rates near 10^5 s^{-1} and plastic strains near ~50% were estimated to be around 180 to 240 MPa, varying in this range with grain orientation [13]. Unfortunately dynamic real-time measurements were difficult with this setup due to diagnostic laser scattering; hence, an additional experimental setup was developed to complement these results.

In the second set of experiments a rippled surface was ablated by a controlled laser pulsed, which launched a rippled shock front to an opposite initially flat diagnostic surface that was monitored in real-time with spatially resolved velocimetry techniques, e.g., line VISAR [14] in addition to Transient Imaging Displacement Interferometry (TIDI) displacement measurements [17]. This setup limited the displacements at the diagnostic surface to a reasonable level for TIDI measurements (~ less than one micrometer). These experiments coupled with analytical and numerical solutions provided evidence that viscous and elastic deviatoric strength affect shock front perturbation evolution in clearly different ways. Particularly, normalized shock front perturbation amplitudes evolve with viscosity (η) and perturbation wavelength (λ) as η/λ, such that increasing viscosity (or decreasing the initial wavelength) delays the perturbation decay [15]. Conversely our experimental data, analysis and simulations show that for materials with elastic yield strength Y the normalized shock perturbation amplitude evolves with $Y\lambda/A_0$, which shows wavelength increases have the opposite effect as in viscous materials and perturbation decay is also dependent on initial amplitude A_0 (viscous materials are independent of this parameter). Materials where strength had clear strain rate dependence, e.g., such as a PTW material law [16], behaved similarly to materials with only an effective yield stress (elastic-perfectly plastic) in the shock front perturbation studies obeying a $Y_{eff}\lambda/A_0$ relationship where Y_{eff} was a constant (near ~400 MPa for Cu for strain rates around 10^6 s^{-1}). Magnitude changes in strain rate would increase Y_{eff} as would be expected from the PTW behavior, but small perturbations (typical of regions behind the shock front) near a mean had little effect.

Additional work based on simulations showed that phase transformation kinetics can affect the behavior of the perturbed shock front as well as the evolution of the RM-like instability that develops due to the imprint of the perturbed shock front on the initially flat surface as the shock breaks out.

Experimental Procedures:

Early experiments consisted of a Richtmyer-Meshkov (RM) like instability as shown in Fig. 1. In these experiments a flyer plate launches a shock wave into a stationary target whose diagnostic surface is rippled and periodically supported with a PMMA window surface. This setup proved successful in producing large repeatable ripple deformations for low shock pressures (~2.7 *GPa*) [13]. Figure 2 shows post-mortem ripple measurements using optical profilometry. As can be seen from the Fig. 2, deformation is dependent on crystal orientation. A more detailed discussion of this experiment can be found in [13].

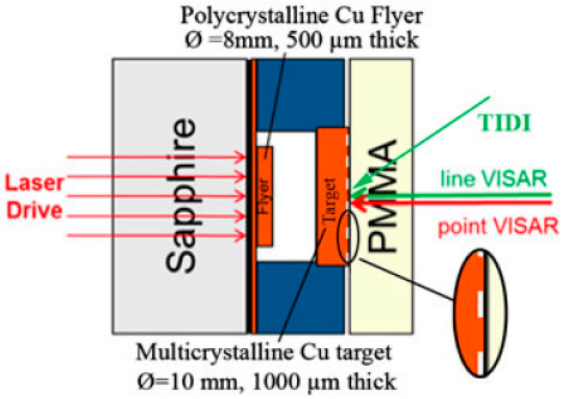

Fig. 1: Experimental setup for early instability experiments. A laser driven flyer launches a shock wave into a partially supported target ripple surface. The impedance periodicity at the ripple surface leads to the formation of large deviatoric deformations useful for material characterization studies.

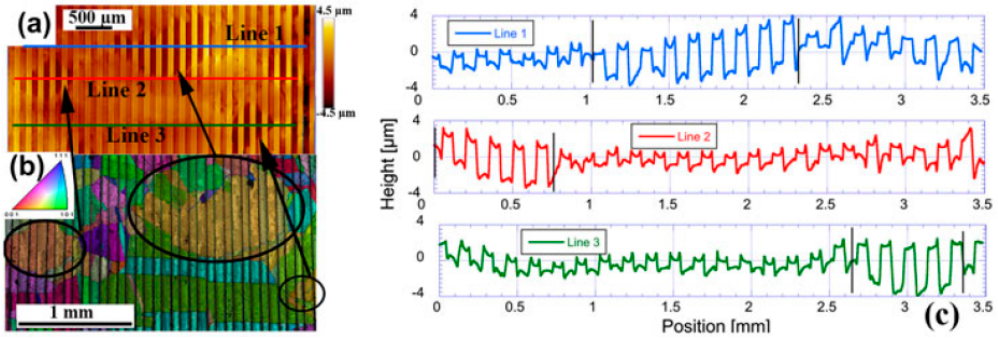

Fig. 2: (a) Optical profilometry of a selected area in the center of a perturbed Cu sample. (b) Inverse pole figure (IPF) map of approximately the same area from EBSD. The color of each grain in (b) corresponds to its out-of-plane crystal directions (the shock direction), as per the stereographic triangle in the inset. (c) Perturbation amplitude profiles along three different locations. Individual grains with large final amplitudes are marked with vertical lines [13].

A drawback of the experiments shown in Fig. 1 was the real-time data acquisition, i.e., transient displacement and velocity diagnostics. The TIDI [17,18] and Line VISAR [14] techniques were not able to capture quality data due to the relatively large initial surface ripples creating too much noise at the imaging camera and dominating over the relative ripple deformations themselves. As a result we moved on to a different experimental setup that will be discussed next to compliment these results.

Our new experiments were based on measurements of displacement and velocity modulations as a rippled shock (generated by direct laser ablation of a rippled surface opposite to the diagnostic surface) arrived at the measurement surface. This is illustrated in Fig. 3 using a simulation of a sinusoidal geometry experiment with the multiphysics code HYDRA [19] that captures laser/ablation dynamics and was used for early experimental design; while subsequent simulations were performed using the finite element code ABAQUS/Explicit™ [20] to facilitate incorporation of various strength models and post processing results.

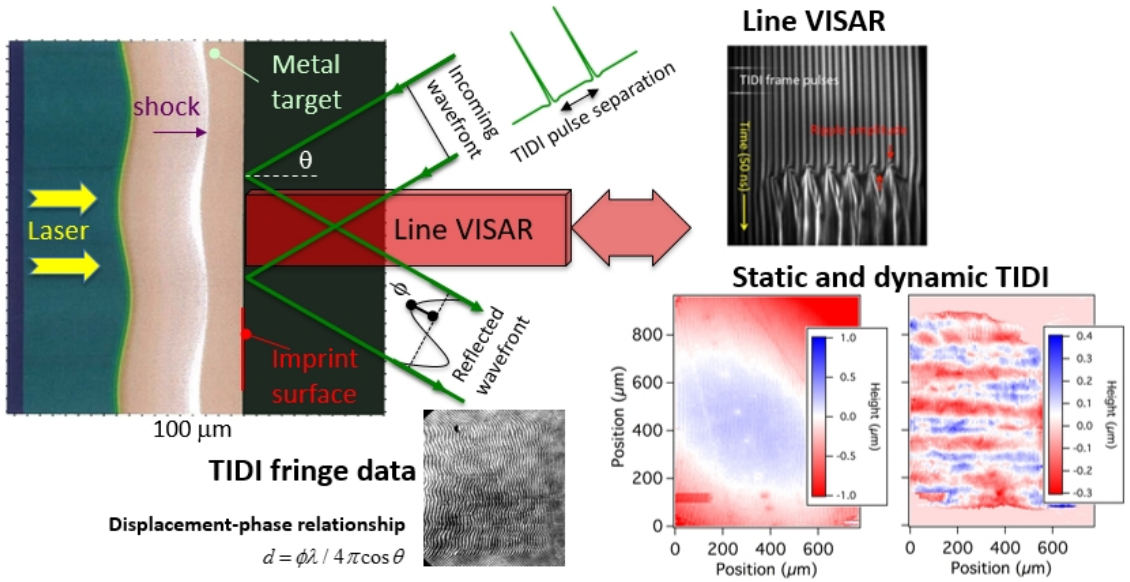

Fig. 3: Experimental setup with directly laser ablated samples. Displacement (TIDI) and velocity measurement (Line VISAR) are made on an initially flat surface that evolves as the rippled shock front breaks out.

Half-hard Oxygen-free high conductivity (OFHC) Cu targets were fabricated, in addition to iron samples from a 99.99% pure iron rod. For the copper samples some bicrystal specimens (to help provide experimental data for orientation dependence), were grown using the vertical Bridgeman technique. A graphite mold was created to pin the grain boundary (GB) in place and hold two single crystal seeds as well as the stock rod. The two single crystal seed directions were chosen so a 45° tilt boundary existed between the two orientations. The mold complete with the stock rod and seeds was then placed inside a furnace with a known temperature profile under ultra-high purity argon until the seed thermocouple read 1084°C. The cool-down process then began, and once the furnace cooled, the boule was removed. The sample was then etched in a dilute nitric acid solution to confirm that the boule was indeed a bicrystal. Figure 4 shows the boule after removal from the furnace. Targets 6 mm in diameter were then extracted from the boule. The boule was cut so the GB would be in the center of the targets. Targets were then polished with 0.05 µm colloidal silica.

Fig. 4. Bicrystal boule.

A photolithography process was also developed to put surface perturbations, or ripples, on the surface of the sample. A square wave typically with 150 μm wavelength was placed on one side of the samples via columnar mask. The patterned side was then etched in a solution composed of 30% iron (III) chloride, 3 – 4% hydrochloric acid, and DI water. Optical profilometry was performed to assure the etching was successful and to obtain the amplitude of the square wave. Amplitudes were measured to be between 4.5 and 6 μm, as shown in Fig. 5.

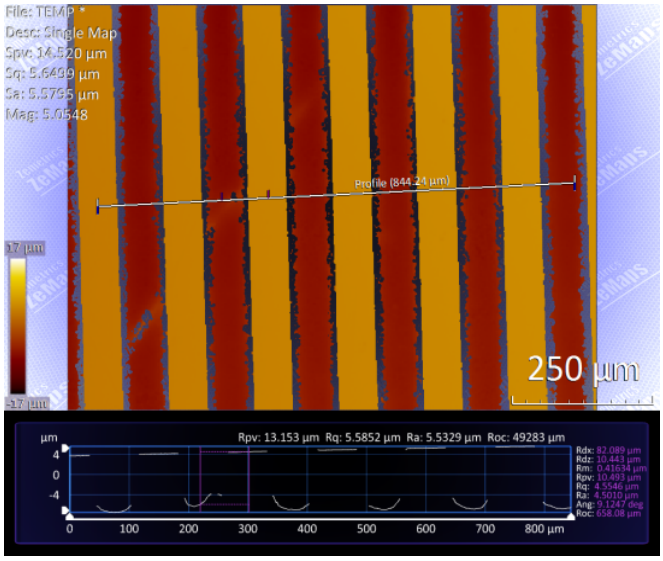

Fig. 5. Optical profilometry of a rippled Cu surface.

Note the square wave in these samples over a distance of about one half a wavelength behaves as a sinusoid, since the square wave contains a spectrum of discrete peaks in Fourier space where the fundamental mode has the wavelength of an equivalent period sinusoid and is followed by an infinite series of exponentially decaying harmonics. As a result, the initially quasi square shock front quickly evolves as it travels the thickness of the sample into a single sinusoidal wave, at about a sample thickness of about half the perturbation wavelength (in our samples *150/2 = 75 μm*) the shock front is essentially sinusoidal and equivalent to a front that would have been created by a similar initial wavelength and amplitude sinusoidal perturbation.

Rippled shocks were generated using 10-30 J square wave pulses of 5 *ns* duration on the modulated target surface from the TRIDENT laser at LANL. First harmonic laser light from the Nd:Glass front-end was converted to 2ω light using monopotassium phosphate (KDP) crystals prior to entering the target chamber. Laser pulses were focused to a 1 mm x 1 mm square spot on the target using a distributed phase plate creating intensities on the target of 4×10^{11} W/cm^2. When the laser first illuminates the modulated surface blow-off plasma creates a separation between the critical surface where the laser is absorbed and the ablation front separating plasma from shocked solid material. With modulations on the ablation front, this scenario quickly sets up the conditions for the ablative RM effect first observed by [21] and

derived theoretically by [22]. When generated in a metal, however, shear flow induced by pressure modulations behind the shock front is opposed by the resulting shear stresses in contrast to inviscid fluids [23]. Note also that any ablation variation (at our power levels) caused by the surface perturbations will be a higher order effect that should not affect the fundamental mode decay over extended distances [24].

In these experiments we investigated two different initial surface perturbation wavelengths (80 and 150 *μm* ±5.0 *μm* with amplitudes of 5 to 6 *μm* ±0.25 *μm*) to study shock perturbation amplitude (i.e., spatial difference between shock fronts in sample) evolution and to study the ensuing dynamic evolution of the post-shock imprint at the initially flat breakout surface. The shock front perturbation (e.g., see Fig. 3 or 11), as it broke out at a free surface, was recorded for several sample thicknesses to determine perturbation evolution with distance traveled Δx. Breakout times were measured using a line-imaging velocity interferometry system (VISAR [14]) that spatially-resolved across several shock front ripples (approximately 1 mm field-of-view and 10 *μm* resolution). An example of typical VISAR rippled shock data is shown in Fig. 3. Most target thicknesses (Δx, ~50 to ~200 *μm*) were chosen such that a clear single mode shock front perturbation would be measured by the VISAR streak camera. The temporal modulation was converted to a spatial amplitude by multiplication with the shock velocity determined from free surface velocity measurements, and a linear U_s - U_p EOS, of separate targets possessing no surface modulation and shot under the same laser conditions (e.g. energy, pulse length). The flat sample VISAR data was also used to convert the laser 5 *ns* pulse to an equivalent (non-square) pressure boundary condition to be used in simulations.

Displacement data obtained from TIDI [17,18] measured the evolution of the free surface with shock breakout. A series of 80 ps probe pulses from the TRIDENT front-end were relayed to the shock breakout surface with a pulse separation of 6.5 *ns*. Changes in surface height topology led to local phase shifts (via optical path length changes) in the target arm of the TIDI Mach-Zehnder interferometer, which produced fringe shifts at the image plane. Two gated, intensified single frame Princeton Instruments (PI-Max 2) cameras were placed at equivalent, but separated image planes created by a 50/50 beam splitter where each camera was timed to capture a separate TIDI probe pulse. An example of raw TIDI data showing the periodic phase shift pattern from the breakout of a rippled shock front is shown in Fig. 3. This surface started as mirror-like where the fringes were initially straight and vertical. The phase is extracted using the method of [25] and then the phase displacement relationship shown in Fig. 3 is applied to provide relative surface heights; one static and two dynamic. Surface height maps for a 150 *μm* wavelength shock ripple given in Fig. 3 show this technique can resolve height features down to ~50 *nm*, and is preferred over integrating VISAR data that can accumulate appreciable errors [2]. A more thorough description of the instrument and analysis of TIDI fringe patterns can be found in [2].

Results: Representative Line VISAR and TIDI results for copper and iron are shown in Figures 6 through 9 for flat and rippled samples. As can be seen in these figures we were able to acquire quality velocity measurements of the flat and rippled samples. Some of the rippled sample VISAR images, however, were difficult to post-process due to significant phase shifts in the interferograms that could not be filtered and unwrapped successfully (e.g., Fig. 9d), nevertheless these images were still valuable for tracking shock front perturbation evolution with distance travelled which will be discussed in more detail later. Fig. 6 and 7 shows typical TIDI results which we were also able to capture with good quality provided surface displacements were under about 1.0 micron [2]. Model development and post processing of the VISAR and TIDI data is discussed next.

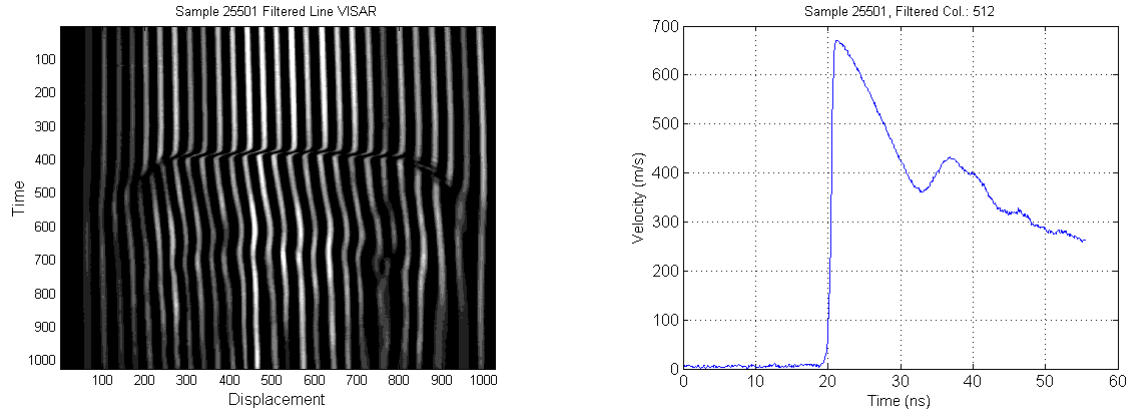

Fig. 6. Copper flat sample 25501 Line VISAR interferogram (left) and velocity history line out (right) from middle of interferogram.

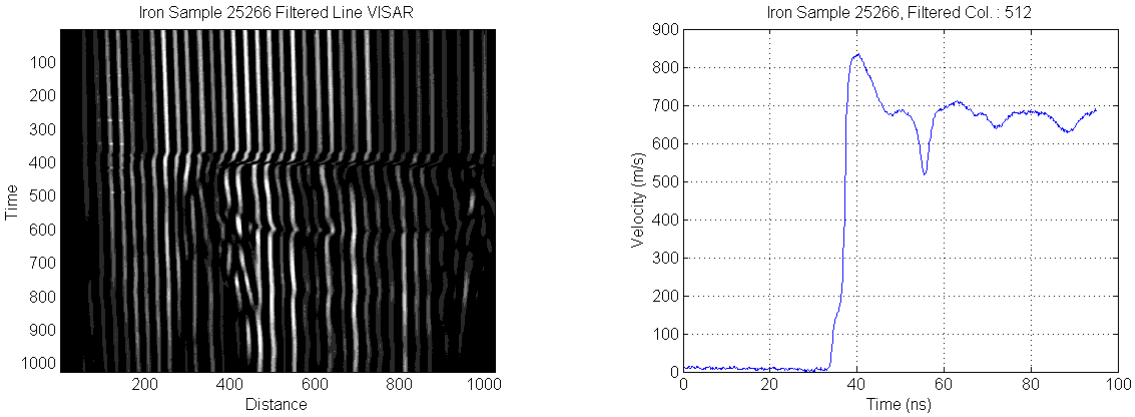

Fig. 7. Iron flat sample 25266 Line VISAR interferogram (left) and velocity history line out (right) from middle of interferogram. Notice clear elastic precursor in velocity history (near ~100 to 150 m/s), but no sign of phase transformation which should appear as a clear discontinuity around ~650 m/s in the velocity history.

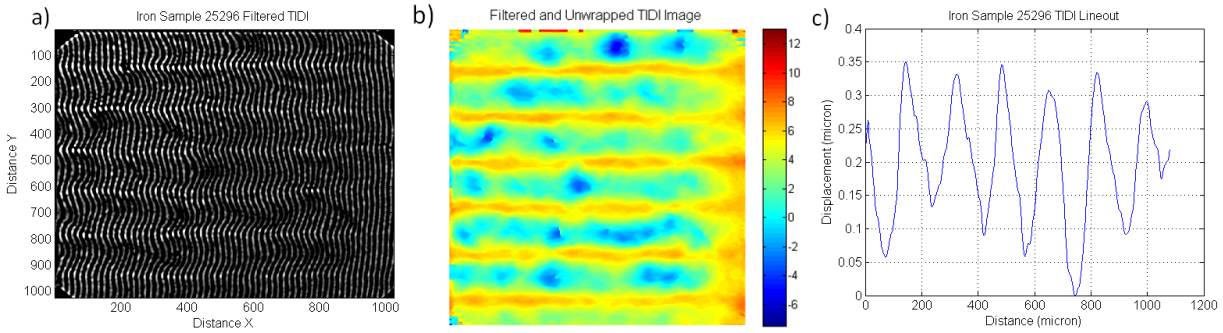

Fig. 8. a) Iron rippled sample 25266 TIDI interferogram and b) post-processed and unwrapped phase contour. Fig. c) shows a lineout from the middle of phase contour image that has been converted to displacement units, where the y-axis is the out-of-plane deformation at the initially flat free surface and the x-axis is the distance along a line on that surface.

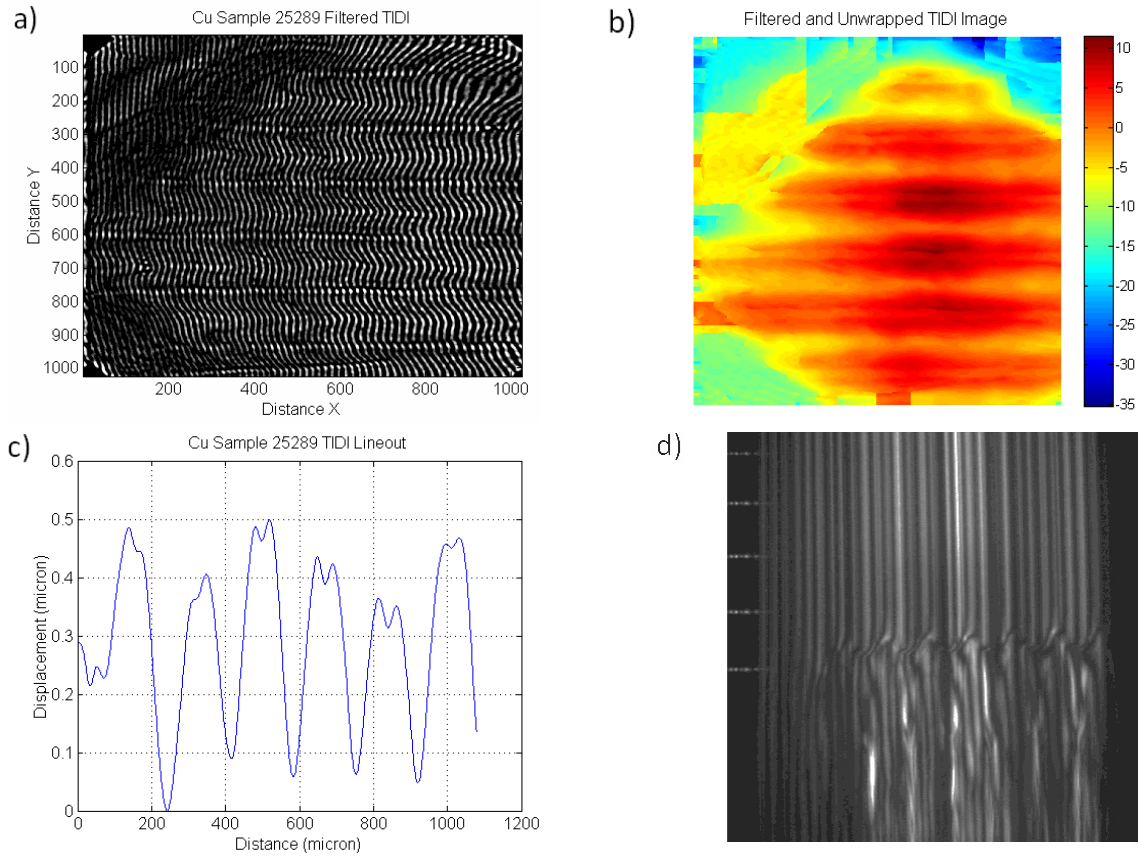

Fig. 9. a) Cu rippled sample 25289 TIDI interferogram and b) post-processed and unwrapped phase contour. c) shows a lineout from the middle of phase contour image that has been converted to displacement units, where the y-axis is the out-of-plane deformation at the initially flat free surface and the x-axis is the distance along a line on that surface. Notice the higher harmonics on the TIDI lineout in c), which are a result of the release wave at the ablated surface reaching and interacting with the now deformed opposite free surface. d) shows a Line VISAR image of the same rippled sample 25289, which is difficult to post-process into velocity line-outs (although possible manually) but is useful for calculating shock front perturbation at breakout.

The VISAR data for the flat sample runs was used to calibrate a PTW [16] strength model for copper and iron. The PTW model was coded as a user subroutine (e.g., VUMAT) into ABAQUS™/Explicit [20]. For iron the subroutine was capable of modeling the low pressure α (BCC) to high pressure ε (HCP) phase transformation that occurs around ~13GPa. Figure 10 shows the results of the simulation results to published experimental data of Barker [26]. The subroutine allowed for each phase to have their own set of PTW parameters, with an equal stress linking assumption when both phases were present at a material integration point at the same time. An additional crystal plasticity code with phase transformation capability was also developed, however, we did not utilize this code beyond preliminary code validation due to a lack of experimental and post-mortem data necessary to calibrate model parameters and to justify the computational cost of the simulations. The final PTW parameters used in the isotropic code are shown in Table 1 and are close to previous published parameters [16,27]. For copper PTW model parameters y_0 = *1e-3* and y_{inf} = *1e-5* (compare to [16]) were adjusted to increase flow stress at low strain hardening values to match our free surface VISAR velocity data on flat samples. In both phases of iron the s_0, s_{inf}, y_0, y_{inf}, and y_1 parameters [16] were all multiplied by 1.75 relative to [27], this has the effect of translating the thermal activation region up along the vertical flow stress axis to better match the elastic precursor seen in our samples.

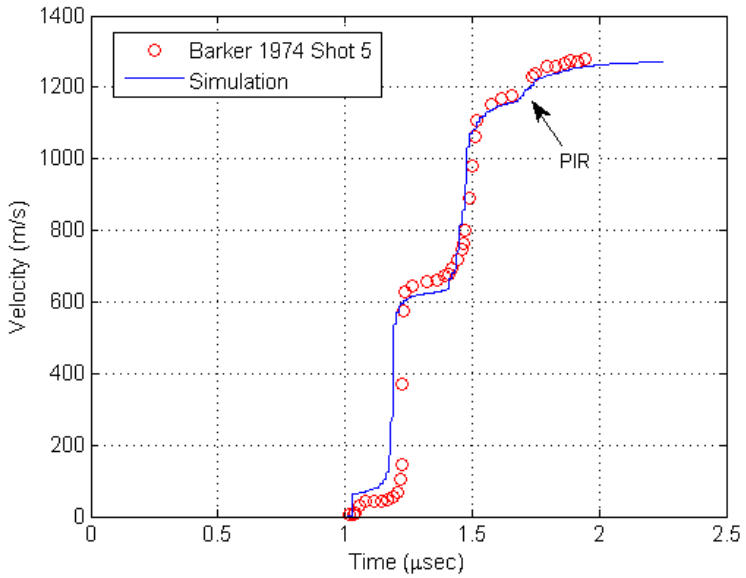

Fig. 10. Comparison of phase aware simulation with published data [26,28]. Material model is integrated into FE software and is capable of using the PTW strength model [16] with different parameters for each material phase. No parameter tuning was made in this example to match this particular data point (i.e. parameters used in simulation were tuned for experimental data gathered in this report instead). The phase interface reflection (PIR) wave is a result of the release wave of the second shock front interacting and partially reflecting at a HCP-BCC phase boundary within the material (i.e., an impedance mismatch), see Barker [26] for more details.

Table 1. PTW parameters calibrated to experimental data generated in this project. Baseline values come from [16,27].

	Fe (BCC)	Fe (HCP)	Cu	Alum
Temperature Constant, κ (-)	3.50e-1	3.00e-1	0.11	0.494
Strain Rate Parameter, γ (-)	1.00e-5	1.00e-5	1.0e-5	1.52e-4
Strain Hardening Parameter, θ (-)	1.50e-2	1.50e-2	2.5e-2	5.29e-2
Strain Hardening Parameter, p (-)	3.00	3.00	2.0	3.0
Saturation Stress Factor, s_0 (-)	1.75e-2	2.1875e-2	8.5e-3	3.2e-2
Saturation Stress Factor, s_{inf} (-)	4.375e-3	4.375e-3	5.5e-4	7.91e-3
Yield Stress Factor, y_0 (-)	6.625e-3	1.1594e-2	1.0e-3	9.42e-3
Yield Stress Factor, y_{inf} (-)	1.1594e-4	1.3125e-3	1.0e-5	5.66e-3
Med. Strain Rate Constant, y_1 (-)	1.75e-2	5.25-2	9.4e-2	1.42e-2
Med. Strain Rate Exponent, y_2 (-)	2.65e-1	2.50e-1	0.25	0.4
Exponent in Drag, β (-)	0.265	0.25	0.25	0.23
Melt Temperature, T_m (K)	1810	2050	1357	930
Reference Shear Modulus, G_0 (Pa)	87.2e9	87.2e9	51.8e9	26.0e9
Pressure Derivative of G, α_P (-)	1.40	1.4	1.36	1.98
G Temperature Parameter, α_T (-)	0.23	0.23	0.43	0.23

The strength parameters for the copper samples were further supported by two additional forms of validation with the rippled sample VISAR and TIDI data. First we looked at the shock front evolution of the perturbed shock front. In this analysis we looked at how the perturbed shock front perturbation amplitude, see Fig. 11, launched from the ablated rippled surface evolves with distance traveled.

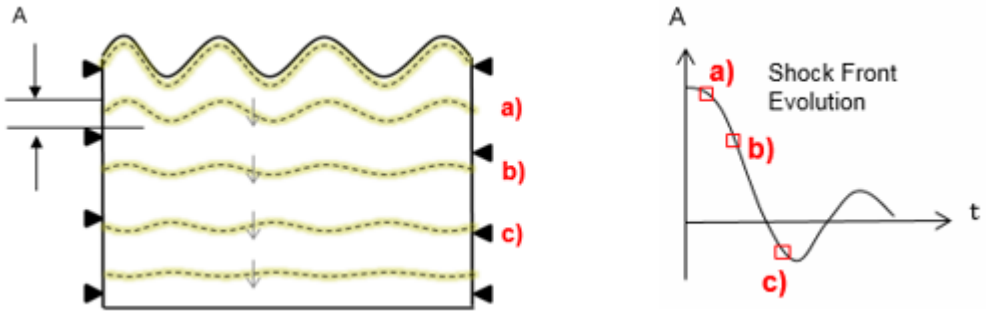

Fig. 11. Perturbed shock front evolution. As the shock front travels the initial perturbation, A_0, decreases, possibly inverts, and approaches a steady amplitude dependent of the material deviatoric strength.

The results of five experiments at similar shock conditions (~12 GPa and 150 *μm* wavelength), where target thickness Δx was varied, are shown in Fig. 12. The error bars are determined by the temporal resolution and noise in the VISAR data. Results at larger $k\Delta x$ values are not included due to perturbation decay being dominated by the shock release wave [29]. In future work, longer laser pulses and thicker samples would be used.

We also show the results of ABAQUS simulations, with a 0.5 micron element size mesh (about 1/10 of initial perturbation amplitude to avoid phase shifts in Fig. 12 plots), where a constant 0.3 *μm/ns* (equivalent to ~12 GPa) velocity was applied to a surface with a perfect sinusoidal modulation (square vs sine perturbation simulations show only minor differences after an initial settling time of approximately half the fundamental mode, and analytically a single sinusoidal geometry is more clearly analyzed). A constant velocity condition was applied to show the decay behavior qualitatively; simulations with release waves did not have an effect on results until the release wave reached the shock front [29]. All simulations used a Mie-Grüneisen equation of state with parameters from [2], but we compare inviscid and viscous fluid solutions to elastic perfectly-plastic and Preston-Tonks-Wallace (PTW) [16] materials possessing strength. For the viscous model a shear viscosity of 10 Pa-s was selected to best fit the shock front width (i.e., rise time) produced by the PTW model. The elastic perfectly-plastic model was given a yield stress of 400 MPa, which was the approximate average flow stress found in the shocked region of the PTW model simulations. These material model parameters were derived from flat sample data; all perturbed sample simulations are predicted using the above material parameters.

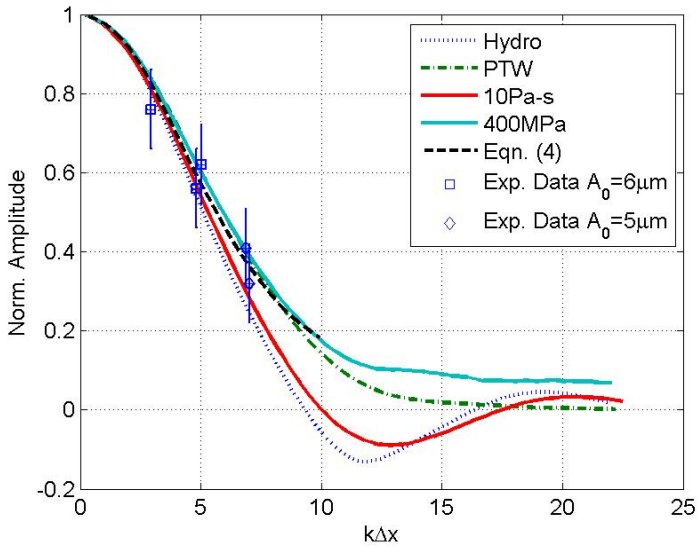

Fig. 12. Shock front perturbation amplitude experimental data and their comparison to inviscid (Hydro), viscous (10 *Pa*-s), elastic-plastic (400 *MPa*), and PTW material models. Simulations are for a 150 *μm* wavelength and A_0 = 6 *μm* initial amplitude.

Figure 12 shows that all the models qualitatively match the perturbed shock front data well, although they differ as the shock perturbation nears inversion, with the strength models predicting no inversion at all. It should be noted that the shock perturbation amplitudes in Fig. 12 were generated by finding the spatial position difference between two particles on the shock fronts that had a particle velocity twice that of the elastic precursor (~0.05 *μm/ns*). The viscous results in Fig. 12 were sensitive to this definition, but consistently showed inversion. Despite the fact that the experimental VISAR

data did not have $k\Delta x$ values large enough to show the predicted difference after inversion, we will show later that highly sensitive displacement measurements (i.e., TIDI measurements) of ripple imprint on the back surface can be used to provide additional material validation information.

Before moving on to the TIDI results we performed some additional analytical work with the perturbed shock front technique, which we show has promise as an experimental tool for characterizing the deviatoric strength of materials in the post shocked state.

To provide additional insight on the role of strength as it pertains to shock front stability up to and near shock front inversion, we present the following semi-analytical model. Zaidel [30], and later Miller [15], used an approximate solution for the shock perturbation amplitude $A(t)$ of a viscous fluid $A(t) = A_{hydro}(t) + A_{pert.}(t)$, where A_{hydro} is the inviscid fluid solution and $A_{pert.}$ is a perturbation caused by the viscosity. We propose a similar form.

Consider that the intensive properties just behind the shock front are comprised of a zeroth order term, which would be the result of a steady shock wave, and a perturbed term, e.g., for the longitudinal velocity we have $v_x = v_{x0} + v_x'$ [15]. Then the equations of motion just behind the shock front after eliminating second order perturbed terms, and noting deviatoric terms are saturated in the shock direction x, are

$$\frac{\partial v_x'}{\partial t} + v_{x0}\frac{\partial v_x'}{\partial x} + \frac{1}{\rho}\frac{\partial P'}{\partial x} = \frac{1}{\rho}\frac{\partial S_{xy}}{\partial y} + \frac{1}{\rho}\frac{\partial S_{xx}}{\partial x} \approx \frac{1}{\rho}\frac{kY}{\sqrt{3}} + 0 \tag{1}$$

$$\frac{\partial v_y'}{\partial t} + v_{x0}\frac{\partial v_y'}{\partial x} + \frac{1}{\rho}\frac{\partial P'}{\partial y} = \frac{1}{\rho}\frac{\partial S_{yy}}{\partial y} + \frac{1}{\rho}\frac{\partial S_{yx}}{\partial x} \approx \frac{-i}{\rho}\frac{kY}{\sqrt{3}} + 0 \tag{2}$$

where S_{ij} is the deviatoric stress, Y is the material yield stress, and we assume perturbed terms vary in the y direction with $exp(iky)$, to account for their periodicity. The terms on the RHS in Eq. (1) and (2) represent the difference between an inviscid material and materials with strength. Along a peak or valley the perturbation amplitude is

$$A(t) = -\int_0^t U_s'(t)dt = -s\int_0^t v_x'(t)dt,\ A(0) = A_0,\ \ dA/dt\Big|_{t=0} = 0 \tag{3}$$

where we have used a linear relationship for the shock velocity perturbation $U_s' = sv_x'$. The RHS of Eq. (1) is of opposite sign to the instantaneous value of v_x', then the strength delays the perturbation decay and an estimate for $A(t)$ before inversion is

$$A(t) = -s\int_0^t v_x'(t)dt \approx A_{hydro}(t) + \frac{1}{2}\frac{U_{s0} - v_{x0}}{U_{s0}}\frac{1}{\rho_0}s\beta k\frac{Y}{\sqrt{3}}t^2 \tag{4}$$

where the second term on the RHS is an estimate for A_{pert} before shock inversion, and we have assumed small density perturbations, i.e., $\frac{v_{x0}}{U_{s0}} \approx 1 -$

ρ_0/ρ. We find that the fitting factor $\beta \approx 0.7$ produces good results across a wide range of pressures, geometries, and strengths if the approximate limits $A_0/\lambda<0.05$ and $PA_0/\lambda>Y$ (P is mean shock pressure) are met and that there is qualitatively agreement beyond these limits [30]. Predictions of Eq. (4), with $A_{hydro}(t)$ obtained from numerical simulations without strength and with $Y = 400$ *MPa*, are included in Fig. 12 until the simulations no longer showed yielding at the shock front inflection points, at which point Eq. (4) is invalid.

A result of Eq. (4) is that care needs to be taken when normalizing experimental perturbation results. In inviscid fluids various geometries will fall on a single perturbation curve for a given shock intensity. For viscous materials the normalization in Fig. 12 leaves a factor of η/λ (where η is viscosity) in the analytical solution of [15,30]. Hence an increase in wavelength will push a point down in Fig. 12. For materials with strength a factor of $Y\lambda/A_0$ is left so that an increase in wavelength or initial perturbation amplitude pushes a point up or down respectively [31]. This suggests sources of deviatoric stress could be validated through initial perturbation amplitude or wavelength changes (we were unable to show this due to a lack of larger $k\Delta x$ values). PTW simulations showed the same approximate dependence on λ/A_0 within the limits mentioned and qualitatively beyond those limits. As a final note, if Miller's [15] Eq. (49) is replaced with our Eq. (1) and (2) then the $Y\lambda/A_0$ factor can be verified with his analytical procedure as well with excellent agreement to ABAQUS simulations. Figures 13 through 15 show simulation and analytical results. Both approaches produce similar results, supporting the $Y\lambda/A_0$ dependence for shock front evolution in materials with elastic strength. This analysis clearly shows that deviatoric resistance, particularly strength or viscosity based, could be validated with perturbed shock front measurements by varying simple experimental parameters such as initial perturbation wavelength or amplitude.

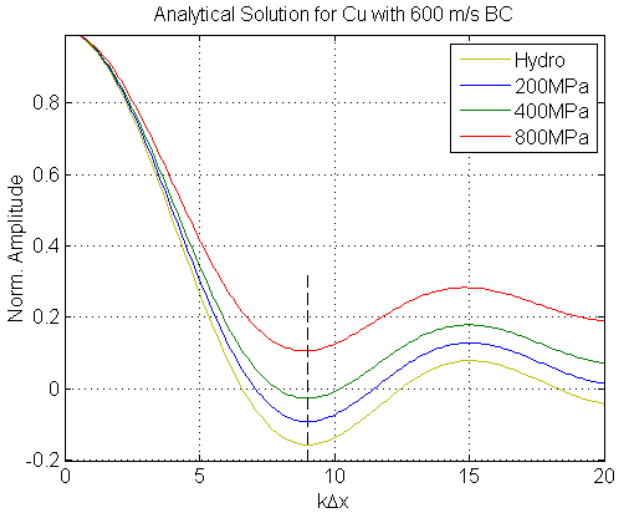

Fig. 13. Analytical shock front perturbation evolution solution based on method of [15,30] with modifications to use an elastic-plastic material strength model and a linear *Us-Up* equation of state. Analytical solution is accurate until material stops yielding, which is approximately at the dashed vertical line, i.e., when the shock front perturbation amplitude is near zero amplitude. Stress values in the legend are the yield strengths used in the solutions.

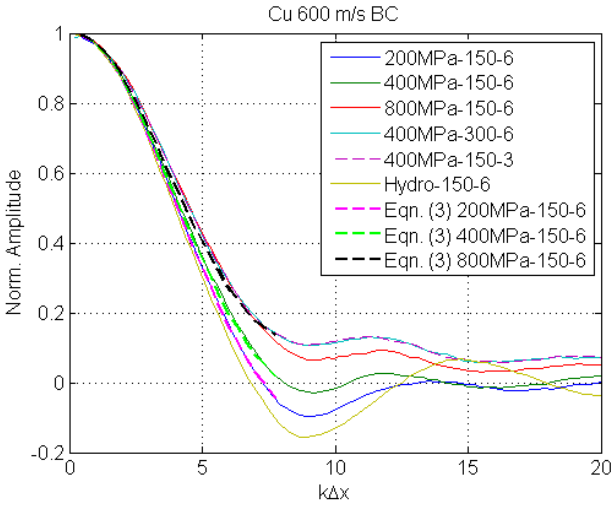

Fig. 14. ABAQUS simulations of shock front perturbation evolution. Simulations and analytical solutions predict that the shock front perturbation amplitude (up to inversion) scales with the material yield strength Y, initial perturbation wavelength λ, and initial perturbation amplitude A_0 as $Y\lambda/A_0$. Legend in figure lists simulations in the format of Y- λ- A_0.

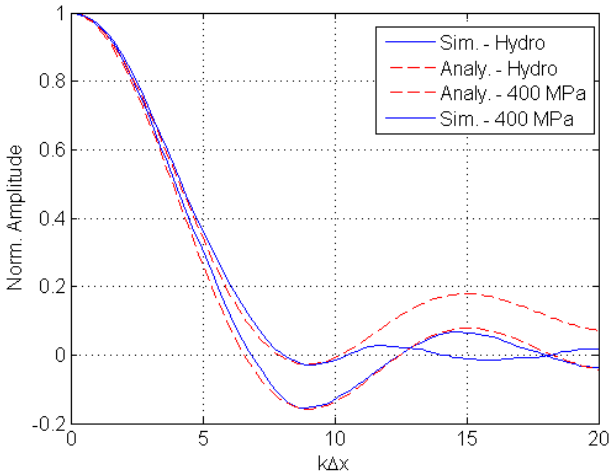

Fig. 15. Direct comparison of analytical and ABAQUS simulations. Analytical solution from [15,30] was improved to model more general equation of states, and materials with elastic strength. Improved analysis is accurate up to ~shock front inversion, while steady state analytical solution provides an upper bound to actual steady-state amplitude. Analytical solution could be modified to more accurately model evolution after shock front inversion with minor modifications.

We used the transient TIDI displacement data to provide additional supporting data for our copper strength parameters. Table 2 lists the peak-to-valley breakout surface displacement data obtained from the first TIDI frame of TRIDENT shot 25288 and 25289 ($k\Delta x$ ~ 5, A0 = 6 *μm*, Δx = 120 *μm*, 12 *GPa*) and compares it to the viscous (10 *Pa-s*), elastic-plastic (400 *MPa*) and PTW model. Figure 16 shows the simulated peak-to-valley evolution for the PTW material for this sample and loading configuration.

Table 2. Experimental peak-to-valley TIDI surface data for shots 25288 and 25289 and simulation predictions. Amplitudes are taken 6.2 and 7.0 *ns* after leading shock breakout respectively.

Time (ns)	Experimental. (*μm*)	Hydro. (*μm*)	Viscous (*μm*)	Elastic-Plastic (*μm*)	PTW (*μm*)
6.2±0.5	0.20±0.05	0.37	0.35	0.26	0.22
7.0±0.5	0.33±0.05	0.53	0.50	0.39	0.32

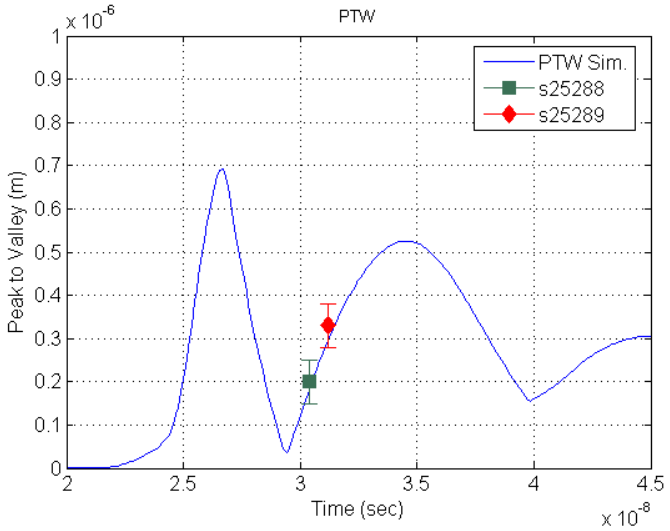

Fig. 16. Experimental TIDI peak-to-valley amplitudes measured at initially flat surface of samples as the rippled shock front breaks out at the free surface for Cu shots s25288 and s25289. Experimental results are compared to ABAQUS™ simulations using the calibrated PTW material strength model.

The only difference between these two shots is the timing of the first TIDI frame capture relative to shock breakout, where the first frame was taken at 6.2 *ns* and 7.0 *ns* for shots 25288 and 25289, respectively. As can be seen in Table 2, the viscous model is significantly off when compared to the experimental data and strength models. The error in the viscous model stems from weak viscous stress as the shock breaks out at the free surface particularly after arrival (~2.5 *ns* after leading shock breakout) of the stronger shock front produced at the thicker section of the sample. By comparison, the models with strength produce strong deviatoric gradients and in this case the saturated longitudinal deviatoric component is relevant since there is a free surface [32]. Increasing the viscosity improved the viscous results, but increased the shock front rise time beyond what experimental VISAR velocity data from flat samples could support. Rise times in the flat samples were around 1.2, 1.0, and 1.7 *ns* for the experimental data, PTW model, and 10 *Pa-s* model, respectively, with uncertainties near ±0.2 *ns*, and doubling the viscosity approximately doubled the rise time. Shock front rise time in the elastic-plastic model (~0.4 *ns*) is limited by artificial viscosity, but outside of this brief high strain event the elastic-plastic model matches the deviatoric stress generated in the PTW model better than the viscous model. Similar agreements between elastic-plastic and more complicated material models were observed in other recent instability studies [33].

Returning to the iron samples we experienced some difficulties observing a clear signal of phase transformation in our samples despite being well above the ~13 *GPa* phase transformation threshold, see for example Fig. 7. In our ~100 micron samples these results predict that the phase transformation kinetics are much slower than previously reported [34,35]. Further analysis and testing is needed to confirm these results and propose possible explanations for the sluggish kinetics. However, our models showed that kinetics of phase transformation can have a meaningful effect on the evolution of the hydrodynamic instability. Phase kinetic parameters for iron were initially set at v = 1e5 s^{-1} and B = 3375 J/kg, where v represents a reference transformation rate and B is akin to an energy barrier [36]. These values reproduced the data in [28] and references therein well. In iron simulations parameters controlling phase kinetics were varied. Faster kinetics led to more uniform pressure contours, having a similar result on transient free surface ripple formation as increasing the strength of the material. All simulations showed smaller permanent deformations, relative to the transient deformations, after the shock release wave reached the free surface. Simulations showed that with a longer pressure (laser) pulse the transient perturbations at the free surface would have grown at a quasi-linear rate typical of small amplitude RM instabilities [37]. Figure 17 illustrates the simulation results, where the 'slow' kinetics had v = 1.00e5 s^{-1} and B = 3375 J/kg.

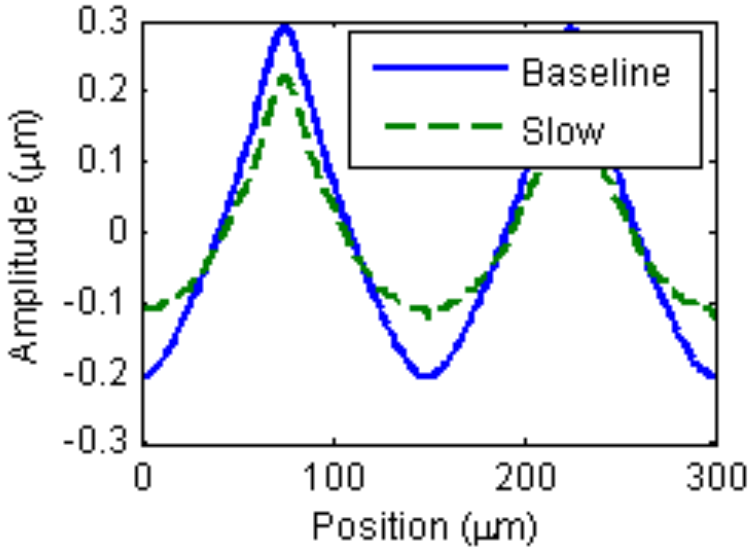

Fig. 17. Iron free surface amplitude simulation results at 9.1 ns since elastic wave breakout.

Characterization of global and local damage: an interesting byproduct of using bicrystalline samples to study RM-like instabilities was the presence of clear damage localization at the boundary. Three bicrystalline samples were characterized: one split boundary, one partially split boundary, and one intact boundary. "Split" refers to the opening of the boundary after the laser ablated the sample. The completely split boundary can be seen in Figure 18. By observing the splitting and incipient spallation at the boundary,

information on how the boundary responds to damage can be obtained. Shot conditions for each of the samples are shown in Table 3.

Table 3. Shot conditions for the rippled bicrystals.

Shot Number/ microstructure	Laser Energy (J)	Pulse (ns)	σ_{Max} (GPa)	σ_{spall} (GPa)
25510/intact	48.3	20	7.69	n/a
25513/split	n/a	20	13.5	5.1
25514/partially split	81.5	20	10.5	n/a

EBSD scans of the 3 sample types can be seen in Figure 18. In sample 25513 where the boundary is completely split, no voids can be seen. This is indicative of the boundary taking all of the damage before spall could occur. Sample 25514 exhibited similar results. The voids also appear to oscillate slightly within the spall plane, which is attributed to the rippled surface.

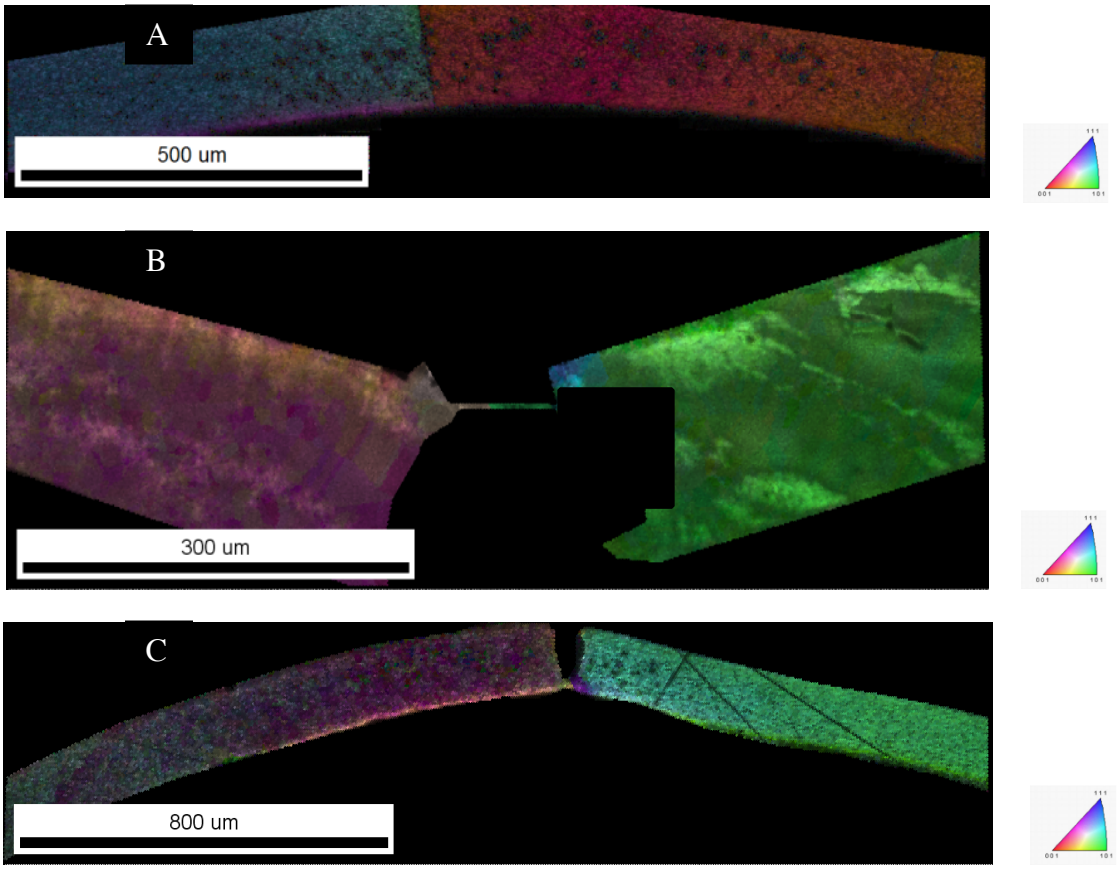

Fig. 18. a) Sample section of 25510, b) Sample section of 25513, b) Sample section of 25514.

From the EBSD scans, it was found that voids nucleated at the boundary, making it a weak point in the sample. The intact boundary shows spall along the boundary and within the bulk of the grain. Samples 25513 and 25514 were shot at higher pressures, and results show that the boundary takes all

of the stress of the shock. This is indicative of fast growth of damage occurring along the boundary.

Velocity and displacement records from the VISAR and TIDI were obtained. Velocity profile is shown in Fig. 19 for 25513. The profiles for 25510 and 25514 look similar in shape to the record shown in Fig. 6. In the record for 25514, there is some rippling below the shock wave. More pronounced rippling in the vertical lines can be seen in the line-VISAR record for sample 25513. Two velocity profiles were taken for 25513, one before the rippling (red line) and one in the middle of the rippling (yellow line) seen in the record. The profile taken from the yellow line exhibits an HEL-like feature and spall pullback. The HEL-like feature may be indicative of the boundary splitting.

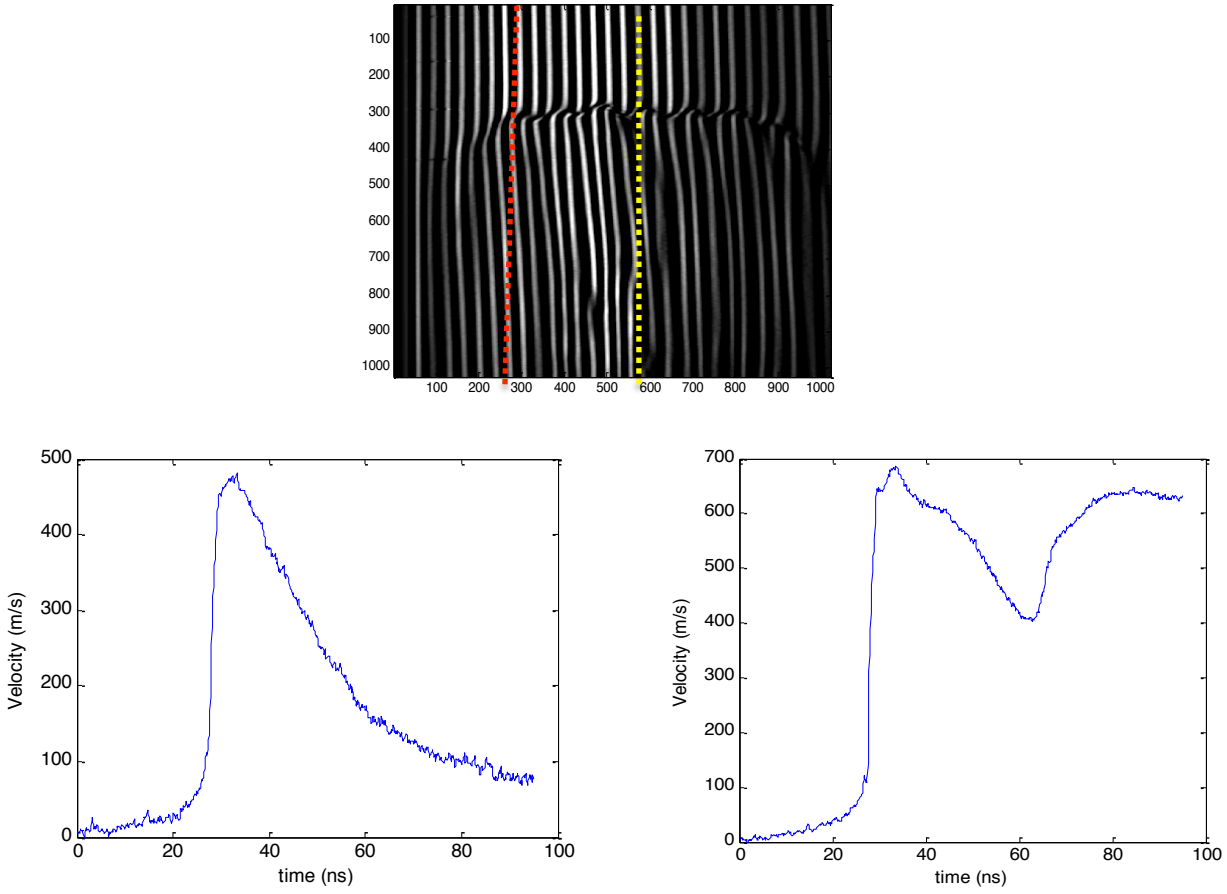

Fig. 19. VISAR results for sample 25513.

TIDI results for sample 25513 can be seen in Fig. 20. A notable feature in the TIDI measurement for sample 25513 is the bulge in the left side of the record. The bulge corresponds to a high displacement on the sample surface, which can be seen in the displacement result. The bulge on the TIDI record can be correlated to the EBSD scan for the sample, where a portion of material is missing in the approximate region corresponding to the bulge.

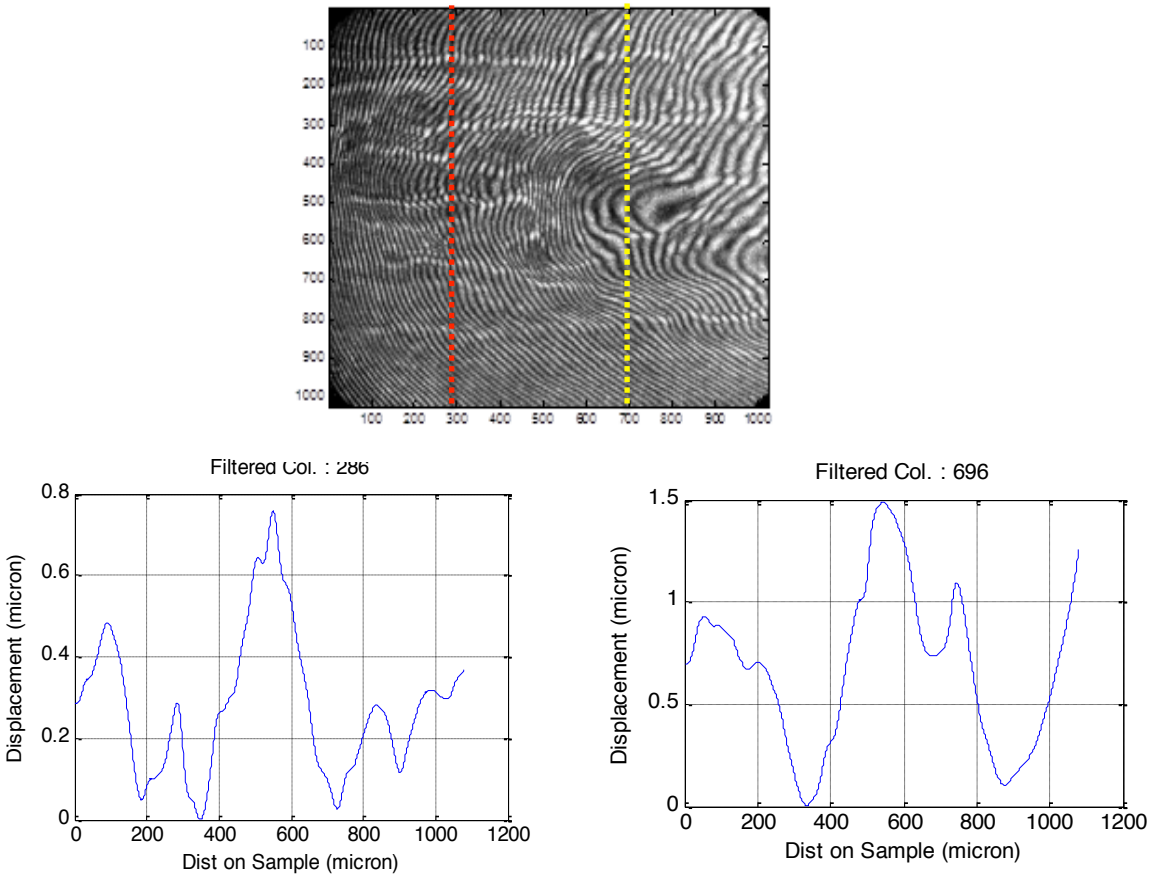

Fig. 20. TIDI results for sample 25513.

Conclusions: In this project we were successful in developing two experimental setups for providing validation data for material strength models and an experimental and analytical framework that can be applied to materials with phase transformations. The partially supported rippled surface experiments (Fig. 1) provided data for relatively low impact velocity experiments typical of single stage gas guns. While dynamic data collection was difficult in this setup we were able to recover targets and gather repeatable post-mortem measurements of ripple deformation. These measurements showed a clear dependence between ripple deformation and grain orientation. We believe similar experiments could be performed with other materials without and with phase transformation capabilities.

An additional set of experiments was also performed with an ablated rippled surface that was used to launch a rippled shock front to an initially flat free surface. In these experiments evolving displacements at the initially flat free surface as the perturbed shock front broke out were kept below a threshold (~ 1 micrometer) that allowed transient velocity (Line VISAR) and displacement (TIDI) data to be accurately collected in real-time. This data was used to support interesting analytical models and simulations of

perturbed shock front evolution. We were able to show that viscosity and strength affect the shock front perturbation evolution in significantly different ways as has also been suggested in other instability studies [38,39]. Furthermore, simulations performed with our phase aware strength models show that phase transformation kinetics can play a meaningful role on the evolution of perturbation amplitudes under hydrodynamic instabilities, in addition to strength effects, so the use of these techniques to estimate strength or validate strength models in the presence of phase transformations must be done with care, and under conditions that insure fast and complete transformation into the phase of interest. On the other hand, the results suggest that this could be an additional tool to study phase transformation kinetics.

Other Collaborations:

Close collaborations were established with a number of LANL staff members, e.g., R. Dickerson (now retired), P. Dickerson (now at Sandia National Laboratory, Albuquerque), and A. Koskelo provided help with sample preparation as well as stimulating discussion. R. Jonhson and T. Shimada at the TRIDENT laser facility at LANL, now close, provided invaluable assistance and insight during the execution of the experiments.

Publications/Presentations:

Publications

• P. Peralta, E. Loomis, Y. Chen, A. Brown, R. McDonald, K. Krishnan and H. Lim. "Grain orientation on dynamic strength of FCC multicrystals at low shock pressures: a hydrodynamic instability study," Phil. Mag. Letters, 2015, 95:67-76.

• S. Opie, S. Gautam, E. Fortin, J. Lynch, E. Loomis, P. Peralta, “Behaviour of rippled shocks from ablatively-driven Richtmyer-Meshkov in metals accounting for strength,” *Journal of Physics*, 2016, 717:012075.

• E. Fortin, S. Opie, A. Brown, J. Lynch, E. Loomis, P. Peralta, “Void Nucleation and Growth at Grain Boundaries in Copper Bicrystals with Surface Perturbations,” ASME IMECE 2016-67649, November 2016.

• S. Opie, E. Loomis, P. Peralta, T. Shimada, R. Johnson, “Strength and Viscosity Effects on Perturbed Shock Front Stability in Metals”, Physical Review Letters, submitted 2016, in second review*.

* This paper has been reviewed, revised and resubmitted, and is currently waiting for reviewer comments on the revisions. It has not been accepted yet. The other articles will be attached as an appendix here, and will be uploaded individually through E-link as well.

Presentations

• K. Krishnan, Y. Chen, S. Gautam, A. Brown, R. McDonald, L. Wayne, E. Loomis, and P. Peralta, “Constitutive Framework for Modeling Incipient Spall Damage in FCC Metals using Microstructurally Explicit 3D Finite Elements.” World Congress on Computational Mechanics. Barcelona, Spain, 2014.

• S. Opie, K. Krishnan, S. Gautam, A. Brown, P. Peralta, E. Loomis, “Crystal Level Phase Transformation with a Dislocation Based Strength Model,” *US National Congress on Computational Mechanics (USNCCM)*, San Diego CA, July 2015.

• S. Gautam, S. Opie, E. Fortin, J. Lynch, E. Loomis, P. Peralta, “Calibration and validation of the PTW dynamic strength model for Cu using novel feedthrough hydrodynamic instability experiments,” *Annual Meeting of the APS Four Corners Section*, Tempe AZ, October 2015.

• S. Opie, S. Gautam, E. Fortin, J. Lynch, E. Loomis, P. Peralta, “Novel Feed-through Richtmyer-Meshkov Instability (RMI) Experiment for Dynamic Material Strength and Phase Transformation Model Validation,” *Annual Meeting of the APS Four Corners Section*, Tempe AZ, October 2015.

• P. Peralta; E. Loomis; S. Opie, S. Gautam, E. Fortin; and J. Lynch, “Feedthru of rippled shocks from ablatively-driven Richtmyer-Meshkov in metals accounting for material strength.” Poster presentation, IFSA Annual Meeting, Bellevue, WA. September 2015.

• S. Opie, S. Gautam, E. Fortin, J. Lynch, “Novel Feed-through Richtmyer-Meshkov Instability (RMI) Experiment for Characterization of Dynamic Material Response,” *APS March Meeting*, Baltimore MD, March 2016.

• S. Opie, D. Kong, E. Fortin, J. Lynch, E. Loomis, P. Peralta, “Effects of Phase Transformation and Dynamic Material Strength on Hydrodynamic Instability Evolution in Metals,” *ASME IMECE 2016-67561, Phoenix, AZ* November 2016.

• E. Fortin, S. Opie, A. Brown, J. Lynch, E. Loomis, P. Peralta, “Void Nucleation and Growth at Grain Boundaries in Copper Bicrystals with Surface Perturbations,” ASME IMECE 2016-67649, November 2016.

• E. Fortin, M. Catlett, J. Lynch, E. Loomis, P. Peralta, “Void Nucleation and Growth at Grain Boundaries in Shock-Loaded Copper Bicrystals,” TMS Annual Meeting. San Diego, CA, February 2017.

• Saul Opie, E. Loomis, E. Fortin and P. Peralta, “Effects of Deviatoric Material Behavior on Hydrodynamic Instability Evolution in Metals.” Poster presentation. JLF/NIF User Group Meeting, February 2017.

Personnel Status:

Name	Institution	Position in project	Country of Citizenship	Status
Pedro Peralta	ASU	Principal Investigator	US	Active
A. Brown	ASU	PhD Student	US	Graduated
Elizabeth Fortin	ASU	PhD Student	US	Active
Saul Opie	ASU	PhD Student	US	Active
Sudrishti Gautam	ASU	MS Student	Nepal	Graduated
Ashish Gopalakrishnan	ASU	MS Student	India	Active
Jenna Lynch	ASU	MS Student	US	Graduated
Y. Chen	ASU	Undergraduate Student	China	Graduated
Dr. Eric Loomis	LANL	Collaborator	US	Active

References:

1. Meyers, M.A., *Dynamic Behavior of Materials*1994, New York: John Wiley & Sons, Inc.
2. Loomis E, Hammerberg J, Cooley JC, Shimada T, Johnson RP, Peralta P, Olson R, Gray III GT. High-resolution measurements of shock behavior across frictional Be/Cu interfaces. Journal of Applied Physics. 2015;117(18):185906
3. Barton NR, Bernier JV, Becker R, Arsenlis A, Cavallo R, Marian J, Rhee M, Park HS, Remington BA, Olson RT. A multiscale strength model for extreme loading conditions. Journal of applied physics. 2011;109(7):073501.
4. J.F. Barnes, P.J. Blewett, R.G. McQueen, “Taylor instability in solids,” J. App. Phys., 1974, 45:727-732.
5. A.R. Piriz, J.J. Lopez, O.D. Cortazar, “Rayleigh-Taylor instability in elastic solids,” Phys. Rev. E, 2005, 72:056313.
6. E.N. Loomis, “LANL/ASU Summit on Richtmyer-Meshkov Strength Project,” LANL, 2014, LA-UR-14-21052.
7. J. Nye, John Frederick, “Physical properties of crystals: their representation by tensors and matrices,” Oxford university press, 1985.
8. T.J. Vogler, L.C. Chhabildas, “Strength behavior of materials at high pressures,” Int. J. of Impact Eng., 2006, 33:812-825.
9. Park HS, Remington BA, Becker RC, Bernier JV, Cavallo RM, Lorenz KT, Pollaine SM, Prisbrey ST, Rudd RE, Barton NR. Strong stabilization of the Rayleigh–Taylor instability by material strength at megabar pressures a. Physics of Plasmas. 2010;17(5):056314.
10. Dimonte G, Frerking CE, Schneider M, Remington B. Richtmyer–Meshkov instability with strong radiatively driven shocks. Physics of Plasmas. 1996 Feb;3(2):614-30.
11. A.J. Mackinnon, P.K. Patel, et. al., "Proton radiography as an electromagnetic field and density perturbation diagnostic," Review of Scientific Instruments, 2004, 75:3531-3536.
12. Barton NR, Bernier JV, Becker R, Arsenlis A, Cavallo R, Marian J, Rhee M, Park HS, Remington BA, Olson RT. A multiscale strength model for extreme loading conditions. Journal of applied physics. 2011;109(7):073501.
13. P. Peralta, E. Loomis, et. al., "Grain orientation on dynamic strength of FCC multicrystals at low shock pressures: a hydrodynamic instability study," Phil. Mag. Letters, 2015, 95:67-76.

14. Celliers PM, Bradley DK, Collins GW, Hicks DG, Boehly TR, Armstrong WJ. Line-imaging velocimeter for shock diagnostics at the OMEGA laser facility. Review of scientific instruments. 2004;75(11):4916-29.
15. Miller GH, Ahrens TJ. Shock-wave viscosity measurement. Reviews of modern physics. 1991 Oct 1;63(4):919.
16. Preston DL, Tonks DL, Wallace DC. Model of plastic deformation for extreme loading conditions. Journal of Applied Physics. 2003 Jan 1;93(1):211-20.
17. Greenfield SR, Swift DC, Koskelo AC. Transient interferometric studies of shocked bicrystals. In Furnish MD, Gupta YM, Forbes JW, editors.AIP Conference Proceedings 2004, (Vol. 706, No. 1, pp. 1269-1272). AIP.
18. S. R. Greenfield, S. N. Luo, D. Paisley, E. Loomis, D. Swift, and A. Koskelo, in Shock Compression of Condensed Matter, edited by M. Elert, M. Furnish, R. Chau, N. Holmes, and J. Nguyen (American Institute of Physics, 2007) pp. 1093{1096.
19. Marinak MM, Haan SW, Dittrich TR, Tipton RE, Zimmerman GB. A comparison of three-dimensional multimode hydrodynamic instability growth on various National Ignition Facility capsule designs with HYDRA simulations. Physics of Plasmas. 1998 Apr;5(4):1125-32.
20. ABAQUS, Finite Element Code, Version 6.14 (Dassault Systèmes Simulia Corp., Providence, RI, USA, 2014)
21. Aglitskiy Y, Velikovich AL, Karasik M, Serlin V, Pawley CJ, Schmitt AJ, Obenschain SP, Mostovych AN, Gardner JH, Metzler N. Direct observation of mass oscillations due to ablative Richtmyer-Meshkov instability in plastic targets. Physical review letters. 2001;87(26):265001.
22. Goncharov VN. Theory of the ablative Richtmyer-Meshkov instability. Physical review letters. 1999;82(10):2091.
23. Ortega AL, Hill DJ, Pullin DI, Meiron DI. Linearized Richtmyer-Meshkov flow analysis for impulsively accelerated incompressible solids. Physical Review E. 2010;81(6):066305.
24. Ishizaki R, Nishihara K. Model of hydrodynamic perturbation growth in the start-up phase of laser implosion. Physical Review E. 1998;58(3):3744.
25. Takeda M, Ina H, Kobayashi S. Fourier-transform method of fringe-pattern analysis for computer-based topography and interferometry. JosA. 1982;72(1):156-60.
26. L. Barker, R. Hollenbach, "Shock wave study of the $\alpha \rightarrow \varepsilon$ phase transition in iron," J. of App. Phys, 1974, 45:4872-4887.
27. J.L. Belof, R.M. Cavallo, et. al. “Rayleigh-Taylor Strength Experiments of the Pressure Induced Phase Transition in Iron,” LLNL-PROC-492911, 2011.
28. J. Boettger, D. Wallace, "Metastability and dynamics of the shock-induced phase transition in iron," Phys Rev. B., 1997, 55:2840-2849.
29. Wouchuk JG, Cavada JL. Spontaneous acoustic emission of a corrugated shock wave in the presence of a reflecting surface. Physical Review E. 2004 Oct 11;70(4):046303.
30. R. M. Zaidel, J. Appl. Math. Mech., 8, 30 (1967).
31. Vogler TJ. Shock wave perturbation decay in granular materials. Journal of Dynamic Behavior of Materials. 2015 Dec 1;1(4):370-87.
32. Piriz AR, Cela JL, Tahir NA, Hoffmann DH. Richtmyer-Meshkov flow in elastic solids. Physical Review E. 2006 Sep 14;74(3):037301.
33. Ortega AL, Lombardini M, Pullin DI, Meiron DI. Numerical simulations of the Richtmyer-Meshkov instability in solid-vacuum interfaces using calibrated plasticity laws. Physical Review E. 2014 Mar 28;89(3):033018.
34. B. Jensen, G. Gray, R. Hixson, "Direct measurements of the $\alpha \rightarrow \varepsilon$ transition stress and kinetics for shocked iron," J. of Appl. Phys, 2009, 105.
35. R. Smith, J. Eggert, et. al., "Time-dependence of the alpha to epsilon phase transformation in iron," J. of App. Phys., 2013, 114.

36. Greeff C, Rigg P, Knudson M, Hixson R and Gray G 2003 *Bull. of Amer. Phy. Soc.* **48.4** p.56.
37. Atzeni S And Meyer-ter-Vehn J 2004 *The Physics of Inertial Fusion* (Clarendon Oxford)
38. Piriz AR, Cela JL, Tahir NA. Comment on “Viscous Rayleigh-Taylor Instability Experiments at High Pressure and Strain Rate”. Physical review letters. 2010;105(17):179601.
39. Park HS, Lorenz KT, Cavallo RM, Pollaine SM, Prisbrey ST, Rudd RE, Becker RC, Bernier JV, Remington BA. Park et al. Reply. Physical Review Letters. 2010;105(17):179602.

APPENDIX

Grain Orientation Effects on Dynamic Strength of FCC Multicrystals at Low Shock Pressures: a Hydrodynamic Instability Study

P. Peralta[1], E. Loomis[2], Y. Chen[1], A. Brown[1], R. McDonald[1], K. Krishnan[1] and H. Lim[1]
1. School for Engineering of Matter, Transport and Energy, Arizona State University. Tempe, AZ 85287
2. Plasma Physics (P-24), Los Alamos National Laboratory. Los Alamos, NM 87544

Abstract

Variability in local dynamic plasticity due to material anisotropy in polycrystalline metals is likely to be important on damage nucleation and growth at low pressures. Hydrodynamic instabilities could be used to study these plasticity effects by correlating measured changes in perturbation amplitudes at free surfaces to local plastic behavior and grain orientation, but amplitude changes are typically too small to be measured reliably at low pressures using conventional diagnostics. Correlations between strength at low shock pressures and grain orientation were studied in copper (grain size ≈ 800 μm) using the Richtmyer-Meshkov instability with a square-wave surface perturbation (wavelength=150 μm, amplitude=5 μm), shocked at 2.7 GPa using symmetric plate impacts. A Plexiglas window was pressed against the peaks of the perturbation, keeping valleys as free surfaces. This produced perturbation amplitude changes much larger than those predicted without the window. Amplitude reductions from 64% to 88% were measured in recovered samples and grains oriented close to <001> parallel to the shock had the largest final amplitude, whereas grains with shocks directions close to <101> had the lowest. Finite element simulations were performed with elastic perfectly-plastic models to estimate yield strengths leading lead to those final amplitudes. Anisotropic elasticity and these yield strengths were used to calculate the resolved shear stresses at yielding for the two orientations. Results are compared with reports on orientation dependence of dynamic yielding in Cu single crystals and the higher values obtained suggest that strength estimations via hydrodynamic instabilities are sensitive to strain hardening and strain rate effects.

Introduction

One fairly unexplored aspect of dynamic plasticity in solids is the effect of material anisotropy on the low shock pressure regime and its potential impact on variability of the local plastic response in polycrystalline materials. This can have important consequences for plasticity-controlled phenomena, such as spall damage. It has been speculated that spall damage can localize (or be absent) at particular grain boundaries (GBs) due to tendencies to localize strain as a consequence of plastic anisotropy [1, 2]. Note that the dynamic yield strength of Cu single crystals is orientation dependent, as shown both through experiments [3] and modeling [4]. An experimental technique to quantify spatial variability of plastic behavior would be quite valuable to study strain localization at GBs and its dependence on grain orientation and anisotropy.

Hydrodynamic instabilities, both Rayleigh-Taylor and Richtmyer-Meshkov (RM), have been shown to be effective tools to infer material strength in solids at high energy densities [5-9] and offer both a complementary measurement and a more direct quantification of material strength effects above the Hugoniot Elastic Limit (HEL) than what is possible from the out-of-plane particle velocity measurements that are typical for shock experiments [8]. Nonetheless, the use of hydrodynamic instabilities for strength measurements at low shock pressures, e.g., less than 10 GPa in Cu, has not been thoroughly explored [7]. Note that even though there are other techniques to measure strength at low pressures [8], the fact that strength can be deduced from

changes in surface perturbation amplitudes makes the hydrodynamic instability technique attractive due to its simplicity as compared to, e.g., gauges to measure lateral stresses, and shock release and reload methods [8], among others. Furthermore, in-situ diagnostics to measure amplitude changes dynamically such as X-ray [6] or proton [5] radiography as well as Transient Imaging Displacement Interferometry (TIDI) [10], make the technique attractive for dynamic strength measurements. However, amplitude changes at low pressures are small at free surfaces, which make measurements using the aforementioned techniques difficult.

The use of TIDI, which is a spatially-resolved, multi-frame in-situ diagnostic capable of measuring out-of-plane displacements with < 100 nm sensitivity and < 5 μm spatial resolution [10, 11], combined with surface perturbations with a wavelength smaller than the grain size, could provide a powerful tool to study spatial variability of dynamic plasticity in crystalline solids due to anisotropy at low pressures, provided the amplitude changes produced by the instabilities could be increased. Studies of this nature have not been carried out using hydrodynamic instabilities to the best of the authors' knowledge.

Study of spall damage phenomena at GBs requires the use of shock loading, and, hence, the RM instability. The work of Piriz *et al* [7] has shown that the difference between the final perturbation amplitude ($\bar{\xi}$) and a reference value (ξ_0) can be approximated as: $\bar{\xi} - \xi_0 \approx 0.58\pi\rho\left(\xi_0 u_p\right)^2 / \left(\lambda S_y\right)$, where ρ is post-shock density, u_p is the particle velocity, λ is the perturbation wavelength and S_y is the material's yield strength. An approximation of the amplitude changes to be expected from RM experiments on single crystal copper can be obtained by first estimating an appropriate value of S_y. This was done here by obtaining the von Mises stress for each crystal orientation using the stresses at the HEL reported in [3] and averaging the results to get a mean value. This procedure gives $S_y \approx 73$ MPa. Then, using ξ_0 and λ from [7] (20 μm and 5 mm), pressure (3.07 GPa), density (9.36 Mg/m^3) and particle velocity (84.5 m/s) from copper spall experiments [2] in the equation given above results in amplitude changes < 0.6 μm. This is within reach of displacement interferometry, but too small to be measured reliably after testing, since other factors, e.g., sample manipulation, might produce larger changes.

The spall experiments described in [2] were performed with flyer plates and used a Plexiglas (PMMA) window, which would result in an Atwood number [9] $A = \left(\rho_{PMMA} - \rho_{Cu}\right) / \left(\rho_{Cu} + \rho_{PMMA}\right) \approx -0.76$ if a perturbed interface had been present between copper and PMMA; hence, experiments using RM in this work were performed using a similar configuration, i.e., the shock propagates in a solid and reaches a perturbed surface [5]. Given that amplitude changes should depend on particle velocity differences between the top and bottom of the perturbation, and that the analysis in [7] indicates a scaling proportional to the square of the initial rate of change of perturbation amplitude, it would seem plausible that the RM effect could be amplified at low pressures by pushing the perturbation tops against a window. This would reduce the particle velocity at those locations upon shock arrival, while keeping the perturbation bottoms as free surfaces, leading to higher particle velocities there and, ultimately, to larger amplitude changes. These changes should, in turn, be affected by grain orientation, provided perturbation length scales are smaller than the grain size.

Experimental Procedures

The hypotheses described above were tested by performing experiments on 10 mm diameter targets taken from a plate of high-purity Hitachi copper (99.995%, half-hard), polished to a thickness of 1 mm (±10%) and finished with 0.05 μm colloidal silica while maintaining faces

parallel within 0.05°. A square, rather than sinusoidal, wave was chosen to maximize the area in contact with the window, and it was manufactured using photolithography and chemical etching. The process resulted in a square surface perturbation with wavelength λ=150 μm and amplitude ξ_0=5 μm, as determined by optical profilometry, which was performed using a Zygo ZeScope optical profiling system. The ZeScope utilizes white LED light to create interference fringes that are used to map the sample surface. Surface analysis was performed using four different magnifications: 3.15, 5, 10, and 12.6x. For high-magnification imaging, a planar fitting correction was used. This fitting correction accounted for the overall curvature of the sample surface, and corrected this to allow for analysis of a "flattened surface".

The analysis in [7] suggests that these dimensions would result in almost double the amplitude change predicted above, due to ξ_0/λ scaling, with everything else being equal and approximating the square perturbation as a sinusoid. Targets were then heat treated at 900 °C for 4 hours under inert gas to grow the grains to an average size of 800 μm, which led to about 5 surface perturbation periods per grain.

The 8 mm diameter flyer plates were harvested from the same copper plate and polished to a thickness of 0.5 mm (±10%). Dynamic testing was conducted at the TRIDENT facility at Los Alamos National Laboratory (LANL) using laser-launched flyer plates [11]. TRIDENT is a Nd:glass laser that operates at a wavelength of 1054 nm and produces a homogenous drive by spatial filtering and focusing of the laser wavefront by random phase plates for uniform flyer plate acceleration. Additional information can be found in [11]. The flyers were mounted to an 8 mm thick sapphire substrate and rested against a confinement layer (Cu disk 0.01-0.05 mm thick) and the assembly was placed in a vacuum chamber (10^{-4}-10^{-5} Torr). An ablative layer on the sapphire substrate launched the flyers via the expansion of high temperature mixtures of vapor and plasma [11], which accelerated the flyers across a 500 μm gap before impacting the target. The perturbed surface of the target rested flush against a flat, 9.53 mm thick PMMA window on the diagnostic side through which the velocity history was recorded using point and line Velocity Interferometry Systems for Any Reflectors (VISARs), and out of plane displacement was monitored with TIDI. The density and impedance of PMMA are lower than those of copper [12], which favor rapid growth of the RM instability. The setup is outlined in Figure 1.

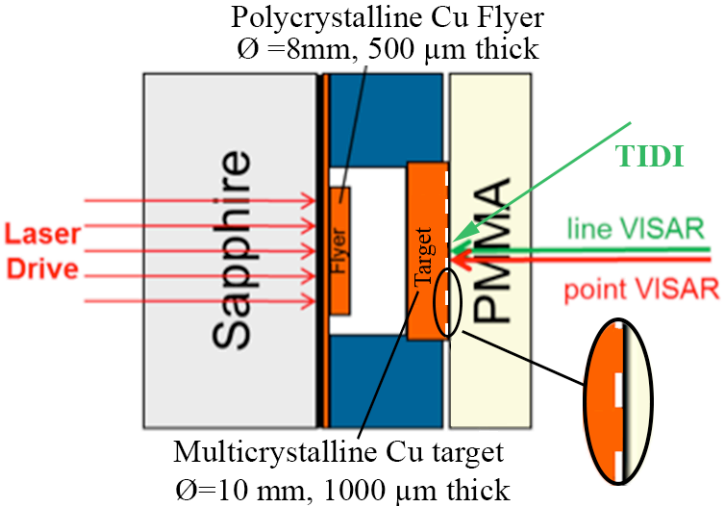

Figure 1. Experimental set-up for RM experiments at TRIDENT. Detail of the interface between the window and the perturbed sample surface is shown in the inset.

Testing was performed at laser energies that produced flyer velocities ≈150 m/s, as measured during experiments without samples where VISAR measurements were made directly on the flyer and by back-calculating the flyer velocity from direct VISAR measurements of particle velocity at the window/sample interface. The calculations were performed using standard hydrodynamic approximations for plate impact experiments that include windows, as shown in [12, 13]. The particle velocity u_p obtained from these calculations were used to estimate the shock stress as $P \approx \rho_o(c_o + s u_p)u_p$ where c_o is the bulk wave speed, s is the slope of the linear U_s-u_p Hugoniot, and ρ_o is the initial density [12], resulting in $P \approx 2.7$ GPa. The flyer velocity also kept the tensile pulse that develops from release waves in this configuration at about the spall strength expected in the samples, i.e., > 2 GPa [1, 13], either precluding spall damage or keeping it at a very incipient stage, while also simplifying the load history analysis of recovered samples. Detailed results from VISAR and TIDI will be reported elsewhere.

The crystallography of the grains in the area of interest was determined using Electron Backscattering Diffraction (EBSD), which was performed at a step size of 5 µm with a Tescan scanning electron microscope, operating at 20 kV and with a 0.75 µm spot size, and an EDAX/TSL OIM™ system.

Results and Discussion

Recovered specimens were examined using optical profilometry to measure the final amplitude of the surface perturbation as a function of position, and the results were correlated with grain crystallography obtained from EBSD, as shown in Figure 2.

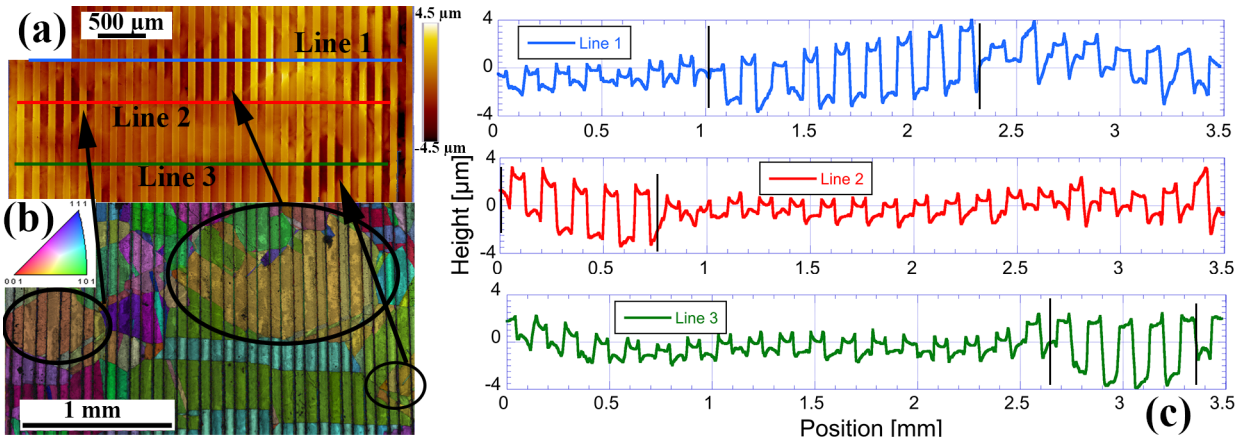

Figure 2. (a) Optical profilometry of a selected area in the center of a perturbed sample. (b) Inverse pole figure (IPF) map of approximately the same area from EBSD. The color of each grain in (b) corresponds to its out-of-plane crystal directions (the shock direction), as per the stereographic triangle in the inset. (c) Perturbation amplitude profiles along three different locations. Individual grains with large final amplitudes are marked with vertical lines. Note that scale bars for Fig. 2a and 2b are different.

Note from Figure 2a that there are regions where the final perturbation amplitude is larger than everywhere else and a comparison with Figure 2b shows that they correspond to individual grains, three of which are highlighted with ellipses. The grain in the lower right corner of Fig. 2a is not fully shown in Fig. 2b; however, the IPF map shows that the grain has an out-of-plane orientation fairly close to the other two. The orientation of these grains parallel to the shock is close to <001>, which has been reported to have higher HEL than other high symmetry

orientations [3]. The grain with large amplitude along line one had a shock direction parallel to <1 7 18> (close to <013>), which is at 22° from <001>, and had a residual amplitude of 1.7 μm (measured from the center of the peak to center of the valley). The smaller grain along line two had a shock orientation parallel to <1 5 14> (also close to <013>), and also had a residual amplitude of 1.7 μm. Note from Figure 2c that these amplitudes are fairly constant through each grain and start changing close to GBs, which suggests that the instability is being affected by the presence of these interfaces. The third grain at the lower right corner of Figure 2a, also had very similar final amplitudes and crystallographic direction as the other two grains. This reproducibility shows the effect is indeed due to grain orientation and that the window amplified the observable amplitude change relative to the predicted value without it.

Some locations had final amplitudes as low as 0.6 μm, such as the center region of line three, which crosses a grain with a shock direction close to <101> (green in Figure 2b). This shows there is a meaningful effect of material anisotropy on final amplitudes in this experiment. Two-dimensional finite element (FE) simulations were used to further study perturbation behavior in these experiments and the effects of the window on the RM instability, using ABAQUS^{TM}/Explicit with an elastic-perfectly plastic model and the Mie-Grüneisen equation of state, following procedures presented in [5, 7]. The following material parameters were used: c_o=3.94 km/s, s=1.49, ρ_o=8.93 Mg/m^3 and G=48 GPa for Cu and c_o=2.6 km/s, s=2.59, ρ_o =1.19 Mg/m^3 and G=1.7 for PMMA, where and G is the shear modulus [12]. The yield strength for PMMA was obtained by extrapolating the results presented in [14], which only covered up to a strain rate of 10^4 s^{-1}, to the strain rate of 10^5 s^{-1} expected in the target/window interface in these experiments, given the results reported in [2], which were performed under conditions similar to those used here. This resulted in $S_y \approx 420$ MPa for PMMA.

The yield strength used for Cu in the model was varied from 120 to 260 MPa in increments of 20 MPa and the simulations were run for 2 μs, which resulted in approximately four full wave transits through the sample so that effects of subsequent loadings after the initial pulse on the surface perturbation amplitude could be evaluated. A "unit cell" representing a full wavelength of the surface perturbation is used in the plane strain simulation that replicates the thickness of both flyer and target. Symmetry boundary conditions are applied on the sides to represent a semi-infinite body. The window is kept thick enough to avoid reflected waves during the simulation time and frictionless contact is assumed between the sample and the window. Figure 3 shows the simulation unit cell with stress contours at different times and amplitudes as a function of time for cases with and without the window and the two values of S_y for Cu that resulted in reasonable matches for the largest and smallest values of final amplitude measured experimentally.

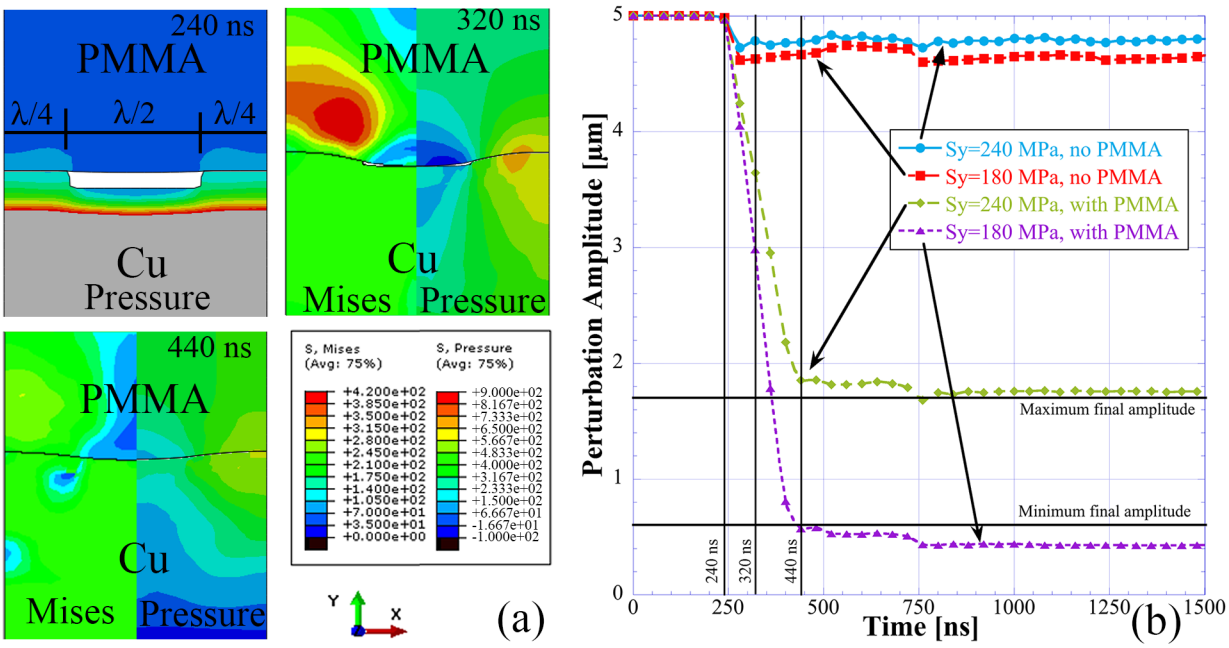

Figure 3. (a) Simulated stress contours (in MPa) for a Cu target with a PMMA window with S_y=240 MPa for copper. Pressure is provided at 240, 320 and 440 ns, while von Mises stress is given only for 320 and 440 ns. The two variables are shown side by side for these times by taking advantage of the symmetry of the model. (b) Simulated perturbation amplitudes for Cu targets with and without windows for two values of S_y for copper.

The stress contours in Figure 3a also show the interaction between the surface perturbation and the window. The shock arrives at the top of the square ripples at about 240 ns, and 80 ns later the window and the bottom of the perturbation touch, leading to further changes in the local pressure distribution that can still be seen at 440 ns. This contact should lead to a reduction in particle velocity at the bottom of the perturbation, and from there the RM instability should proceed, approximately, with A≈-0.76. However, the rate of change of perturbation amplitude is not affected significantly. This is because the window is already moving along the $+y$ direction by the time contact occurs, with velocities of up to 100 m/s according to the simulations. Therefore, the stresses on the window when the valley makes contact are not as high as they would be if its velocity were equal to zero at contact. This explains why both pressure and von Mises stress at this location are lower in the window than in Cu, as can be seen both at 320 and 440 ns (recall that only σ_{yy} needs to be continuous at the sample-window interface). The resulting pressure gradient encourages perturbation growth, leading to changes in amplitude larger than what would be possible without the window. However, the effect is transitory and the simulation indicates that pressure and plastic strain start to equilibrate after 440 ns, which is consistent with the fact that changes in amplitude saturate quickly after that (Figure 3b).

The amplitude changes predicted by the FE simulations for the Cu samples with no windows and S_y=240 MPa (top curve), were in the same order of magnitude as those predicted from the analysis in [7], which indicates that it can be applied to non-sinusoidal, periodic perturbations. The changes for S_y=180 MPa are also small, as expected due to the low shock pressure used. The curves for the same values of S_y when the window is used show that even a window with low impedance, as compared to that of Cu, can make a tremendous difference on the RM instability, when used as it was done in this here. The amplitude change for S_y=240 MPa with the window is

15 times larger than without it, and almost 12 times larger for S_y=180 MPa. Furthermore, large changes stop at around 440 ns, which is within the duration of the initial pulse, so effects from long load history are not likely to be important when the window is present, since most of the amplitude change occurs during the first pressure pulse.

The yield strengths that produced the closest matches in final amplitudes to the measured values were 240 MPa for the largest amplitude, found in grains closer to <001> and 180 MPa for the smallest one, found in grains close to <101>. These values are larger than dynamic yield strengths deduced from HEL measurements for <100> and <101> Cu single crystals [3]. Comparisons of these results needs to be done carefully, since elastic anisotropy in the single crystals changes the amount of deviatoric stress available for each orientation, as shown in [3]. The <100> crystals have the largest HEL because the deviatoric stress is the lowest for a given pressure, whereas the opposite is true for <111>, which actually has a larger von Mises stress than <100> and <101>, so yielding is reached at a lower HEL.

Note, however, that yield stress is not an actual property in single crystals, since it depends on the direction in which is measured [15]. A more appropriate parameter to describe the onset of plasticity in single crystals that obey Schmid's law is the resolved shear stress (RSS) [15] and will be used here to make comparisons with results presented in [3], where it was shown that the RSS at the HEL for all Cu single crystal orientations was approximately the same. Hence, stress tensors at the HELs corresponding to the estimated values of S_y were obtained, to estimate the value of the maximum RSS for the two grain orientations found here leading to maximum and minimum residual amplitudes. The procedure is based largely on the methodology presented in [3] and will be summarized next.

First, the anisotropic elastic constants are rotated from the frame given by the principal axes of the unit cell to the frame defined by the crystallographic orientations of the grains analyzed here, as measured using EBSD [3, 16]. Then, the simulations were used to obtain the normal stress parallel to the shock direction (x_2=y in Fig. 3) at the HEL (σ_{22}^{HEL}), which was 433 MPa for S_y=240 MPa and 295 MPa for S_y=180 MPa, respectively. These stresses are used to estimate the normal strain parallel to the shock direction at the HEL (ε_{22}^{HEL}) assuming uniaxial strain conditions [3, 12], via the following equation [3]:

$$\varepsilon_{22}^{HEL} = \sigma_{22}^{HEL} / C'_{2222} \tag{1}$$

where C'_{2222} is the corresponding elastic stiffness expressed in the grain orientation frame. Once ε_{22}^{HEL} is known, the other components of the stress tensor at the HEL can be calculated as [3]

$$\sigma_{ij}^{HEL} = C'_{ij22}\varepsilon_{22}^{HEL} \tag{2}$$

Where i, j go from 1 to 3. The stress tensors were then used to obtain the maximum RSS for each orientation, by calculating the traction vector on the slip plane defined by its normal **n** ({111} family for FCC copper) and finding the component of that traction vector along the slip direction **b** ($<\bar{1}10>$ family for FCC copper) [3], i.e.,

$$RSS^{(\alpha)} = \sum_{i=1}^{3}\sum_{j=1}^{3}\sigma_{ij}^{HEL} n_j'^{(\alpha)} b_i'^{(\alpha)} \tag{3}$$

where α goes from 1 to 12 to represent all possible slip systems in copper and **n**$'$ and **b**$'$ are the slip plane normal and slip direction unit vectors, respectively, expressed in the grain orientation frame. The maximum RSS among the 12 slip systems is then taken as the critical value to trigger yielding. This led to RSS values of 110 MPa for the <013> orientation and 65 MPa for the <101> orientation, i.e., increases of 5 and 3 times as compared to the value of 22 MPa reported in [3]. The fact that RSSs deduced here are much larger than those in [3] must be a consequence of strain hardening and strain rate effects during perturbation growth. In this regard, the simulations indicate that, plastic strain in the perturbation at 440 ns is rather large, i.e., of von Mises plastic strain of more than 25% in average for the peaks and above 5% for the valleys. Strain hardening of Cu single crystals under quasistatic axial loads can lead to flow stress increases of several fold for these strain levels [17], which is consistent with results shown here.

In addition, the simulations indicate that these levels of plastic strain are about an order of magnitude larger than in the bulk, which suggests that the strain rate in the perturbation is at least one order of magnitude larger as well. A quick analysis of the results presented in [3] suggests that the macroscopic strain rate at the HEL in those experiments is similar to the value expected here, i.e., ~ 10^5 s^{-1}. This is also the strain rate at which copper has been shown to have an increase in strain rate sensitivity [18]. Data shown in [18] suggests that copper experiences an increase of about 50-70% in flow stress when the strain rate goes from 10^5 s^{-1} to 10^6 s^{-1}. Hence, both strain hardening and strain rate effects will lead to increases in flow stress, but the estimations given above suggests that strain hardening has a larger contribution. This, in turn, suggests that flow stresses deduced from the elastic-perfectly plastic model are likely estimates of the *average* values over the evolution of the perturbation, rather than *initial* values. The results reported in [3] reflect the latter, since they were measured from the HEL.

Analysis of time resolved diagnostics is currently underway to try to shed more light into this issue. In particular, velocimetry from VISAR is unlikely to add more information, as preliminary analysis indicates that the technique was not able to resolve the differences in velocity between the peaks and the valleys of the perturbation expected here, which is crucial to follow the time evolution of the perturbation amplitude. The TIDI diagnostic is far better suited for this measurement and the rate of change of perturbation amplitude measured with this technique might provide additional information on effects of flow stress evolution on hydrodynamic instabilities, when coupled with suitable models capable of accounting for strain hardening and strain rate sensitivity effects. This work is in progress.

Conclusions

- Experiments and modeling results have shown that variability on local plastic response in crystalline materials can be studied using the RM instability at low shock pressures by a creating a partial bimaterial interface at the perturbation with a low impedance window. This amplifies the rate of change of perturbation amplitude so that measurements as a function of position can be performed reliably on recovered samples.
- The changes of perturbation amplitude measured experimentally are strongly correlated to local grain orientation and reproducibility of the results was demonstrated as three grains with approximately the same crystal orientation parallel to the shock had similar final amplitudes.
- Values of yield strength leading to maximum and minimum values of the final perturbation amplitude measured in the experiments were estimated using FE models with fairly simple constitutive assumptions typically used to analyze this type of experiments. The stress tensors at the HEL for these values of yield strengths were then used to obtain maximum values of RSS for the two grain orientations with minimum and maximum final amplitudes. The resulting values

suggest that strength estimations via the RM instability do reflect strain hardening and strain rate effects of the material and that anisotropy plays an important role. However, the simplicity of the FE models used makes the estimates semi-quantitative, at best, as far as grain orientation effects are concerned. Additional experiments and analysis are being performed using fully anisotropic models to further refine the understanding of these effects.

Acknowledgements
This work was supported by the Department of Energy (DOE), under Grants # DE-NA0002005 from National Nuclear Security Administration (NNSA) and DE-SC0008683 from the Office of Fusion Energy Science to Arizona State University and an agreement between the DOE Office of Fusion Energy Science and LANL. We gratefully acknowledge the use of facilities with the LeRoy Eyring Center for Solid State Science the Mechanical Testing Laboratory at Arizona State University, as well as access to the TRIDENT laser user facility at LANL.

References

1. Escobedo, J.P., Cerreta, E.K., Dennis-Koller, D., Trujillo, C.P., and Bronkhorst, C.A.: Phil. Mag., 2013. **93**(7): p. 833-846.
2. Wayne, L., Krishnan, K., DiGiacomo, S., Kovvali, N., Peralta, P., Luo, S.-N., Greenfield, S., Byler, D., Paisley, D., McClellan, K.J., Koskelo, A., and Dickerson, R.: Scripta mater., 2010. **63**: p. 1065-1068.
3. Jones, O.E. and Motes, J.D.: J. Appl. Phys., 1969. **40**(12): p. 4920-4928.
4. Dupont, V. and Germann, T.C.: Physical Review B, 2012. **86**(13): p. 134111.
5. Dimonte, G., Terrones, G., Cherne, F.J., Germann, T.C., Dupont, V., Kadau, K., Buttler, W.T., Oro, D.M., Morris, C., and Preston, D.L.: Physical Review Letters, 2011. **107**(26): p. 264502.
6. Park, H.-S., Remington, B.A., Becker, R.C., Bernier, J.V., Cavallo, R.M., Lorenz, K.T., Pollaine, S.M., Prisbrey, S.T., Rudd, R.E., and Barton, N.R.: Phys. Plasmas, 2010. **17**(5): p. 056314.
7. Piriz, A.R., López Cela, J.J., Tahir, N.A., and Hoffmann, D.H.H.: Physical Review E, 2008. **78**(5): p. 056401.
8. Vogler, T.J. and Chhabildas, L.C.: Int. J. Impact Eng., 2006. **33**(1-12): p. 812-825.
9. Buttler, W.T., Oró, D.M., Preston, D.L., Mikaelian, K.O., Cherne, F.J., Hixson, R.S., Mariam, F.G., Morris, C., Stone, J.B., Terrones, G., and Tupa, D.: J. Fluid Mech., 2012. **703**: p. 60-84.
10. Greenfield, S.R., Swift, D.C. and Koskelo, A.C.: AIP Conf. Proc., 2004. **706**: p. 1269-1272.
11. Paisley, D.L., Luo, S.N., Greenfield, S.R., and Koskelo, A.C.: Rev Sci Instrum, 2008. **79**(2 Pt 1): p. 023902.
12. Meyers, M.A., *Dynamic Behavior of Materials*. 1994, New York: John Wiley & Sons, Inc.
13. Peralta, P., DiGiacomo, S., Hashemian, S., Luo, S.-N., Paisley, D.L., Dickerson, R., Loomis, E., Byler, D., McClellan, K.J., and D'Armas, H.: Int. J. Damage Mech., 2009. **18**: p. 393-413.
14. Richeton, J., Ahzi, S., Vecchio, K.S., Jiang, F.C., and Adharapurapu, R.R.: Int. J. Solids Struct., 2006. **43**(7-8): p. 2318-2335.
15. Dieter, G.E., *Mechanical Metallurgy*. Third Edition ed. 1986, New York, NY: McGraw-Hill.

16. Nye, J.F., *Physical Properties of Crystals*. 1985, New York: Oxford University.
17. Anand, L. and Kothari, M.: J. Mech. Phys. Solids, 1996. **44**(4): p. 525-558.
18. Armstrong, R.W. and Walley, S.M.: Int. Mater. Rev., 2008. **53**(3): p. 105-128.

Figure captions

Figure 1. Experimental set-up for RM experiments at TRIDENT. Detail of the interface between the window and the perturbed sample surface is shown in the inset.

Figure 2. (a) Optical profilometry of a selected area in the center of a perturbed sample. (b) Inverse pole figure (IPF) map of approximately the same area from EBSD. The color of each grain in (b) corresponds to its out-of-plane crystal directions (the shock direction), as per the stereographic triangle in the inset. (c) Perturbation amplitude profiles along three different locations. Individual grains with large final amplitudes are marked with vertical lines. Note that scale bars for Fig. 2a and 2b are different.

Figure 3. (a) Simulated stress contours (in MPa) for a Cu target with a PMMA window with S_y=240 MPa for copper. Pressure is provided at 240, 320 and 440 ns, while von Mises stress is given only for 320 and 440 ns. The two variables are shown side by side for these times by taking advantage of the symmetry of the model. (b) Simulated perturbation amplitudes for Cu targets with and without windows for two values of S_y for copper.

Behaviour of rippled shocks from ablatively-driven Richtmyer-Meshkov in metals accounting for strength

S Opie[1], S Gautam[1], E Fortin[1], J Lynch[1], P Peralta[1,a], and E Loomis[2]

[1]School for Engineering of Matter, Transport and Energy, Arizona State University, Tempe, AZ 85287, USA

[2]Plasma Physics (P-24), Los Alamos National Laboratory, Los Alamos, NM 87544, USA

[a]email: pperalta@asu.edu

Abstract. While numerous continuum material strength and phase transformation models have been proposed to capture their complex dependences on intensive properties and deformation history, few experimental methods are available to validate these models particularly in the large pressure and strain rate regime typical of strong shock and ramp dynamic loading. In the experiments and simulations we present, a rippled shock is created by laser-ablation of a periodic surface perturbation on a metal target. The strength of the shock can be tuned to access phase transitions in metals such as iron or simply to study high-pressure strength in isomorphic materials such as copper. Simulations, with models calibrated and validated to the experiments, show that the evolution of the amplitude of imprinted perturbations on the back surface by the rippled shock is strongly affected by strength and phase transformation kinetics. Increased strength has a smoothing effect on the perturbed shock front profile resulting in smaller perturbations on the free surface. In iron, faster phase transformations kinetics had a similar effect as increased strength, leading to smoother pressure contours inside the samples and smaller amplitudes of free surface perturbations in our simulations.

1. Introduction

Hydrodynamic instabilities are a dominant feature of many High-Energy-Density (HED) systems [1]. The growth of these instabilities depends on material phase and intrinsic fields that perturb the hydrodynamics away from an ideal fluid flow [2-4]. Many materials can retain significant resistance to shear deformation at the large strain rates developed under large transient pressure conditions [5]. This strength is known to decrease Rayleigh-Taylor (RT) and Richtmyer-Meshkov (RM) instability growth rates relative to those under ideal hydrodynamic conditions [3-5]. Little is known, however, about the effects of material strength on these instabilities as phase boundaries (solid-solid, solid-liquid, etc.) are approached. Specifically, the behaviour of shock and release waves undergo sharp changes near these boundaries [6], suggesting that significant changes to the growth rate of instabilities may occur at perturbed solid-state interfaces. It is also likely that material strength could mitigate instability growth in inertial confinement fusion (ICF) capsules using metal ablators [7]. Here we describe a novel experimental setup for validating and calibrating material models in loading regimes typical of hydrodynamic instabilities in solids. We study two materials, copper to explore material strength sensitivity, while iron is used to study phase transformation effects from the α to ε transition [6].

2. Experimental Details

Shock experiments were conducted via laser ablation of a sample's free surface as shown in Figure 1a. Pressure was controlled by varying the laser intensity, which determined material strength/phase regimes the sample experienced during loading. Laser pulses lasted for about ~ 7 ns and produced pressures from 10 to 30 GPa. Two sample geometries were used. Flat samples with an approximate 100 μm thickness were tested first and used to correlate a known laser intensity pulse and resulting velocity history at the opposite free surface, to a pressure boundary condition (BC) via simulation. The laser BC to pressure BC calibration was performed with a range of laser energies. All free surface velocities were recorded with a Line VISAR (Velocity Interferometer System for Any Reflector).

Another set of samples had the ablated surface perturbed with a square wave, as shown in Figure 1a, by a photolithography process [8]. Samples had wavelength (λ), amplitude (η), and thickness (t), of approximately 150 μm, 20 μm, and 100 μm, respectively. The perturbations produced a rippled shock front that imprinted the initially flat free surface with a perturbation at breakout. This, in turn, resulted in an RM instability. Out-of-plane displacement measurements were recorded at the free surface with Transient Imaging Displacement Interferometry (TIDI) [9], as seen in Figure 1b. Only two framing cameras were used to obtain two dynamic images per sample. Free surface velocity was monitored with Line VISAR (Figure 2a). The use of TIDI was of interest in this experiment because it provided an alternative for capturing the RM instability evolution. Other instability studies [3] have used radiography, which is not as sensitive to the small displacements seen here. All experiments were carried out at the TRIDENT Laser Facility at Los Alamos National Laboratory (LANL).

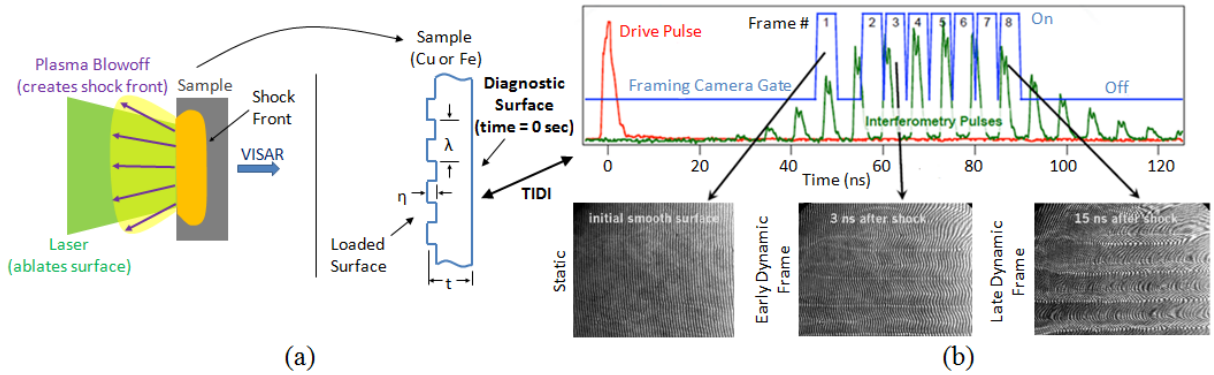

Figure 1. Schematic of experimental setup and diagnostics. (a) Laser ablation and sample configuration. (b) Pulse train of laser illumination to capture raw TIDI data with framing cameras.

3. Experimental Results

Figure 2 shows typical experimental results obtained with the VISAR and TIDI diagnostics. Figures 2a and 2b (raw VISAR images) are interferograms of a line on the diagnostic surface (x-axis) with time (y-axis). A vertical line out of post-processed Line VISAR interferograms produces a velocity history (Figure 2c) of a particular point on the diagnostic surface. The velocity histories of flat samples (Figures 2b and 2c) have the usual form seen in laser ablation or plate impact experiments, i.e., the surface accelerates and decelerates as a whole with the shock front and release wave respectively. The free surface of the perturbed samples, however, evolves from an initially flat surface (Figure 2d) to a perturbed surface (Figures 2e and 2f) with a wavelength equal to the etched perturbations that were laser loaded. The perturbations evolve higher harmonics with time due to interactions with the release wave. Note that Figures 2d and 2e are post-processed displacement plots from raw static and dynamic images (interferograms) similar to those in Figure 1b.

4. Simulation Results and Discussion

Two dimensional, plane strain simulations were performed to assess sensitivity of the behavior to strength and phase transformation properties. Calculations were carried out in ABAQUS/Explicit™,

via a user material subroutine (VUMAT) with a model similar to that used in [10]. An equation of state (EOS) [11] was used for the volumetric response and a Preston-Tonks-Wallace (PTW) model for the deviatoric response [12]. In iron, the phase transformation kinetics followed the phenomenological model shown in [13]. Separate EOS and strength parameters were used for each phase.

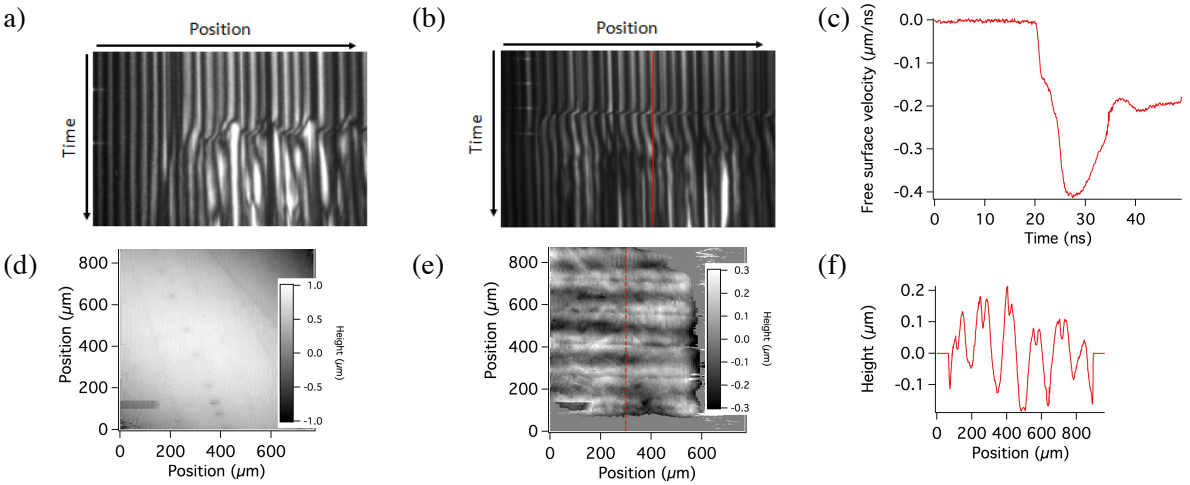

Figure 2. Typical experimental data. (a) and (b) raw Line VISAR of perturbed and flat Cu samples respectively. (c) Line out of flat sample Line VISAR data. (d) Pre-shot TIDI data of perturbed sample. (e) Dynamic TIDI data of perturbed sample. (f) Line out of dynamic TIDI data.

Copper and iron unitless PTW parameters were initially taken from literature [12,14] and adjusted to match the shock front profiles from the flat sample VISAR records. For both phases of iron the s_0, s_{inf}, y_0, y_{inf}, and y_1 parameters [12] were multiplied by 1.75 relative to [14]. This translated the thermal activation region up along the vertical flow stress axis to better match the elastic precursor seen here. In copper, y_0, y_{inf}, and y_2 were changed from 1e-4, 1e-4, and 0.575 to 1e-3, 1e-5, and 0.250, respectively, which increased the initial yield stress and kept the saturation stress unchanged. Strain rate sensitivity and phonon drag characteristics were the same for both materials as in [12] and [14].

Phase kinetic parameters for iron were initially set at ν = 1e5 s^{-1} and B = 3375 J/kg, where ν represents a reference transformation rate and B is akin to an energy barrier [13]. These values reproduced the data in [6] and references therein well. However, for our relatively thin samples changing B to 688 J/kg (or ν to ~1e7 s^{-1}) reproduced velocimetry data better, suggesting a very fast transformation (~1 ns), defined as a 95% transformation at the large driving forces used here [15]. More work is needed to understand the discrepancy in B, i.e., a better kinetics model may be needed.

Tables 1 and 2 show peak-to-peak (P-P) amplitudes obtained from perturbed sample TIDI data and from simulations using the parameters calibrated to flat sample VISAR data. These baseline parameters were used to look at the perturbation growth sensitivity to in material parameters. For copper, the strain rate sensitivity was increased (~2x) and decreased (~0.5x) by likewise changes in the $\varkappa$ and β PTW values [12] relative to the baseline, while other PTW values were changed to retain similar quasistatic strength across all simulations. As shown elsewhere [3] strength parameters were found to have a significant effect, simulations showed that the perturbed shock front profile traveling through the sample was less perturbed in samples with increased strength. In iron simulations parameters controlling phase kinetics were varied. Faster kinetics led to more uniform pressure contours, having a similar result on transient free surface ripple formation as increasing the strength of the material. All simulations showed smaller permanent deformations, relative to the transient deformations, after the shock release wave reached the free surface. Simulations showed that with a longer pressure (laser) pulse the transient perturbations at the free surface would have grown at a quasi-linear rate typical of small amplitude RM instabilities [2]. Figures 3 and 4 illustrate the simulation results, in Figure 4 the 'slow' kinetics had ν = 1.00e5 s^{-1} and B = 3375 J/kg.

Table 1. Cu (s25288, 19J) amplitudes, experimental and baseline simulation results.

Time[a] (ns)	Experimental Amplitude P-P (microns)	Simulation Amplitude P-P (microns)
6.2	0.20 +/- 0.05	0.18
12.7	0.65 +/- 0.05	0.62

a. Time since shock breakout.

Table 2. Fe (s25293, 55J) amplitudes, experimental and baseline simulation results.

Time[a] (ns)	Experimental Amplitude P-P (microns)	Simulation Amplitude P-P (microns)
9.1	0.48 +/- 0.07	0.50
28.2	0.15 +/- 0.05	0.17

a. Time since elastic wave breakout.

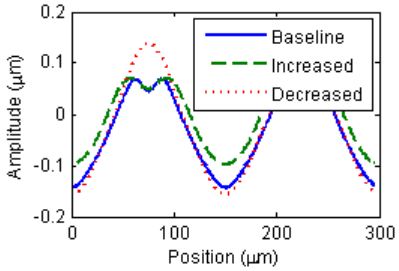

Figure 3. Copper free surface simulations results at 6.2 ns since shock breakout.

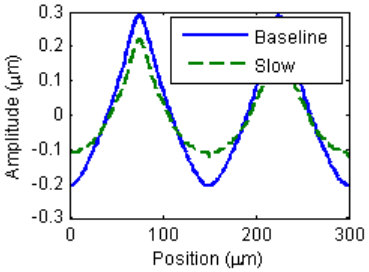

Figure 4. Iron free surface amplitude simulation results at 9.1 ns since elastic wave breakout.

5. Conclusions

Anticipation and control of hydrodynamic instabilities is critical in many applications, particularly ICF design. To accurately predict instability evolution a comprehensive material model is needed that accounts for the wide variation in strength and phases that evolve with the loading conditions. We have described a novel experimental setup that provides data to validate material models/parameters in high strain rate and pressure regimes typical of hydrodynamic instabilities in solids. Preliminary experiments and simulations show that experimental results of this setup are sensitive to material properties controlling strength and phase kinetics, and are useful for supplying additional experimental data for model validation in addition to typical velocity measurements, e.g., Line and Point VISAR.

References

[1] Zhou C and Betti R 2007 *Phys. Plasmsa* **14** 072703
[2] Atzeni S And Meyer-ter-Vehn J 2004 *The Physics of Inertial Fusion* (Clarendon Oxford)
[3] Park H et al. 2010 *Phys. Rev. Lett.* **104** 135504.
[4] Ortega A et al. 2015 *J. Mech. Phys. Solids* **76** p.291
[5] Barton N and Rhee M 2013 *J. App. Phys.* **114** 123507
[6] Boettger J and Wallace D 1997 *Phy. Rev. B* **55** p.2840
[7] Loomis E et. al. 2010 *Phys. Plasmas* **17** 056308
[8] Peralta P et. al. 2015 *Phil. Mag. Lett.* **95** p.67
[9] Greenfield S et. al. 2000 *Laser-Induced Damage in Optical Mat.* **4065** p.557
[10] Zuo Q, Harstad E, Addessio F and Greeff C 2006 *Mod. Sim. Mat. Sci. Eng.* **14** p.1465
[11] Heuze O 2006 *AIP Conf. Proc.* **845** p.212
[12] Preston D, Tonks D and Wallace D 2003 *J. App. Phy.* **93** p.211
[13] Greeff C, Rigg P, Knudson M, Hixson R and Gray G 2003 *Bull. of Amer. Phy. Soc.* **48.4** p.56
[14] Belof J et. al. 2012 *AIP Conf. Proc.* **1426** p.1521
[15] Jensen B, Gray G and Hixson R 2009 *J App. Phy.* **105** 103502

Acknowledgments

This work was supported by the US Department of Energy, Office of Fusion Energy Science under grant # DE-SC0008683. Access to the TRIDENT facility at LANL is gratefully acknowledged as well.

Proceedings of the ASME 2016 International Mechanical Engineering Congress & Exposition
IMECE2016
November 11-17, 2016, Phoenix, Arizona, USA

2016-67649

VOID NUCLEATION AND GROWTH AT GRAIN BOUNDARIES IN COPPER BICRYSTALS WITH SURFACE PERTURBATIONS

Elizabeth V. Fortin
Arizona State University
Tempe, Arizona, USA

Saul Opie
Arizona State University
Tempe, Arizona, USA

Andrew D. Brown
The University of New South Wales, UNSW Canberra
Campbell, ACT, Australia

Jenna M. Lynch
Arizona State University
Tempe, Arizona, USA

Eric Loomis
Los Alamos National Laboratory
Los Alamos, New Mexico, USA

Pedro D. Peralta
Arizona State University
Tempe, Arizona, USA

ABSTRACT

Material failure on the microstructural level is important in determining macroscale behavior. When a material is subjected to dynamic (shock) loading conditions, damage and deformation patterns due to spall failure can provide a basis for connecting micro- to macroscale behavior. By analyzing deformation patterns at and around interfaces and boundaries that are representative of those found in engineering materials at high strain rates, we can develop stronger structures that can withstand impact collisions and rapid crack propagation. The addition of surface perturbations to one side of the samples provides insight on how strain localization occurs during the shock loading process and how the rippled release wave interacts with the boundary. Copper bicrystal samples were grown from two single crystal seeds using the vertical Bridgeman technique. A photolithography process was developed to create periodic surface perturbations on one side of the samples. The square wave ripples had a 150 μm wavelength and 5 μm amplitude. The bicrystals were shocked using laser ablation on the perturbation side at the Trident laser at Los Alamos National Laboratory and monitored using a VISAR (velocity interferometer systems for any reflector) and TIDI (transient imaging displacement interferometry) system. Shock pressures used were around 8 – 10 GPa. Targets measured 5 mm in diameter and 100 microns thick. The orientations of the grains were [001] and [111] along the shock direction with a 50° misorientation angle for the boundary, which was aligned parallel to the shock direction. Samples were soft recovered and cross-sectioned to perform quantitative characterization of damage using electron backscattering diffraction (EBSD) and Scanning Electron Microscopy (SEM) to gather information on the characteristics of the grain boundary and its surroundings, with emphasis on how the rippled surfaces and material anisotropy affected strain localization and spallation, initial results show that damage indeed localized at the grain boundary and that surface perturbations led to heterogeneity of spall damage distribution in the grain bulks.

INTRODUCTION

Shock loading can lead to several failure modes, including spallation. The process of spallation is caused by the superposition of tensile release waves created when the shock front reaches the free surface. The tensile stress produced by this superposition can exceed the strength of the material, inducing void nucleation, growth, coalescence, and separation. Pressure, pulse duration and shape of the shock wave have an effect on how voids form, as well as material variables such as constitutive properties, microstructure, and anisotropy [1 - 5]. The purpose of this work is to explore the effect the square wave ripples have on strain localization, and spallation in copper bicystals. By observing single boundaries in copper bicrystals, the kinetics of nucleation and growth of damage at the boundary can be studied. The addition of surface perturbations provides insight on how strain localization occurs during the shock loading process via its effects on the development of hydrodynamic instabilities during compression and as fiducials to monitor the deformation behavior close to the boundary as compared to the grain bulks. Also, the presence of these surface perturbations leads to spatial heterogeneities on the release waves, which can then interact with the boundary in novel ways.

Terminated twins and grain boundaries with misorientation angles in the 25° to 50° and 55° to 60° range are

preferred sites for intergranular damage nucleation [4]. In work by Wayne [4, 8], it was found that the 60° twins (Σ3) were damaged often but at a lower frequency than that of which they were present in the microstructure, i.e., the fraction of damaged boundaries that were twins was less than the overall fraction of damaged and undamaged boundaries that were twins. Therefore, this signified that the 60° twins (Σ3) are strong boundaries. Results in [4] were reaffirmed and further expanded upon by Brown et al. [5, 9] with experiments on heat treated and fully recrystallized samples. Research performed on copper bicrystals observed that the grain with more slip systems active during impact will contain more damage [10], proving that crystallographic orientation influences damage nucleation. The orientation of the two grains in the bicrystal, [100] and close to [111], was chosen for analysis because they have the lowest and highest longitudinal wave speed, the highest and lowest spall strength among high symmetry orientations [14], and low and high Taylor factors in copper, respectively. With these differences, the mismatch on behavior across the boundary should be at maximum. The misorientation angle for the boundary was 50°, so spall should localize at the boundary.

The work presented in this study aims to identify how the surface perturbation affects void nucleation and growth. The ripples also allow the effect of strain localization at the boundary to be observed. The experimental procedures performed to achieve these aims are outlined in the next section.

EXPERIMENTAL PROCEDURE

All targets were cut from a copper bicrystal grown from Hitachi copper (99.995%, half hard) using the vertical Bridgeman technique. The orientations of the seeds were [001] and in between [111] and [110] in the shock direction. A 50° misorientation angle was measured across the boundary. Figure 1 shows the bicrystal that was grown. The boundary shown is parallel to the shock direction and naturally meandering, which resembles boundaries found in natural poly- and multicrystals. The colors of the grains change slightly in the stitched image due to a slight variation in the tilt of the sample. However the tilt is not large enough to greatly change the orientations of the grains.

Figure 1: IPF map of the bicrystal used for experiments. Colors correspond to directions perpendicular to the boundary plane.

Both sides of the samples were polished to 0.05 µm colloidal silica to prepare the surface for the addition of perturbations. A square wave with a 150 µm wavelength was patterned on one side of the polished surface via a columnar photomask. Ripples were placed perpendicular to the boundary so the effect of the shock wave across the rippled boundary could be measured at more than one site. The patterned side of the targets was then etched using a solution composed of 30% iron (III) chloride, 3 – 4% hydrochloric acid, and DI water. After etching, optical profilometry using a ZeScope was performed to determine the amplitude of the square wave. Amplitudes were measured to be 4.5 – 6 µm, as shown in Figure 2.

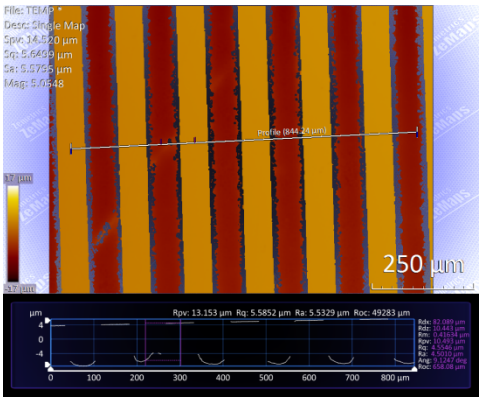

Figure 2: Profilometer results of bicrystal ripples

Shock waves were created by using the Trident laser at Los Alamos National Laboratory (LANL) to shock the bicrystal target via direct laser ablation. The Trident laser facility houses a Nd: glass laser driver with a fundamental wavelength of 1054 nm. Additional information on Trident can be found in [13]. Pulse duration varied for each sample and frequency doubling was used to get a green light. A phase plate was also used to homogenize the beam over a 1 x 1 mm^2 region. The rippled side faced the laser while the flat side was used as the diagnostic side for the line-VISAR and TIDI. Ripples were placed vertically in the holder. Velocity and surface displacement data from experiments were captured using VISAR and TIDI techniques, respectively. Laser interferometry is a well-established tool for obtaining a velocity vs. time profile of the target. TIDI employs a technique that encodes phase information in high spatial frequency interference fringes and shows the surface displacement of the sample in the out of plane direction. More information on line-VISAR, or ORVIS, and TIDI can be found in [11] and [12], respectively.

Test conditions were designed so the tensile pressures were above the spall strength of multicrystalline copper. It has been proven in Kenal et al. [13] and Minich et al. [14] that copper samples with smaller grain sizes had a lower resistance to spall, thus the bicrystalline samples, with two large grains, should have a higher spall strength. Targets for post-shot analysis were chosen based on their line-VISAR record and condition. Three samples were characterized in this study: one split boundary, one partially split boundary, and one intact boundary. The splitting refers to the opening of the boundary after the laser ablated the sample, shown in Figure 3, which is an indication of spall damage localization at the grain boundary of the bicrystals. Table 1 gives the testing conditions for the selected samples. Pulse duration was held constant at 20 ns and the laser energies were 48.3 and 81.5 J for 25510 and 25514, respectively. Laser energy was unable to be recorded for 25513.

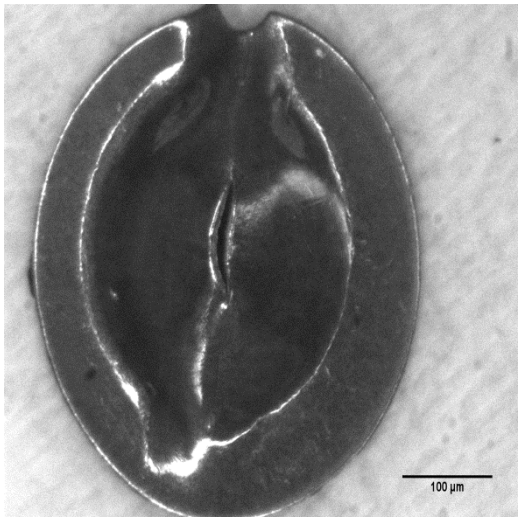

Figure 3: Unzipped boundary of sample 25513. Image is taken of the backside/free surface of 25513. Magnification: 10x.

The selected samples were examined using optical microscopy, scanning electron microscopy (SEM), and electron backscattering diffraction (EBSD) to characterize the microstructure. Targets were cross-sectioned using electrical discharge machining (EDM) and mounted in epoxy to be polished to EBSD quality. In order to study the effect the boundary had on void nucleation and to characterize the unzipping of the boundary, samples were consecutively sectioned for 2-D EBSD analysis. Each grain the EBSD technique identifies is assigned a single average orientation within a 5° tolerance. This results in misorientation angles below 5° not to be included in statistical analysis and an overall error of ±5°.

RESULTS AND DISCUSSION

Observing the unzipping and incipient spall at the boundary is important in understanding the combined effects of the grain boundary and surface perturbations on the spall process. If the sample has partially or completely split at the boundary, as shown in Figure 4, it is not possible to observe spallation at the boundary, as no voids are present.

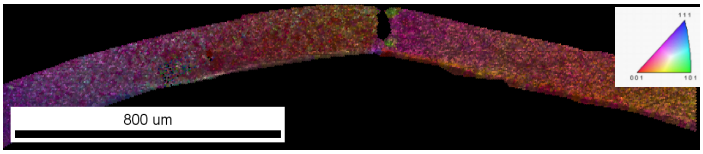

Figure 4: Example of a partially unzipped boundary in sample 25514

The EBSD map of the structure shown in Figure 4 is an image quality (IQ) map overlay on top of the scan. By doing this, the voids around boundary can be seen.

Velocity data from the line-VISAR for samples 25510, 25513, and 25514 are shown in Figures 5 – 7. The velocity obtained for 25513 (completely unzipped sample) shows a very clear profile. The HEL-like feature and possible spallation point after the peak velocity can be observed. It is possible that the HEL-like feature was caused by the perturbations on the shock front at breakout. Both the completely and partially unzipped boundaries in samples 25513 and 25514 respectively show a bottoming out in the velocity profile. Compared to flat copper samples shocked at laser energies close to the three samples presented in this study, the velocity of 25510 is less than its flat counterpart shot. Line-VISAR data for flat samples shot near 81.5 J were unable to provide accurate results for comparison.

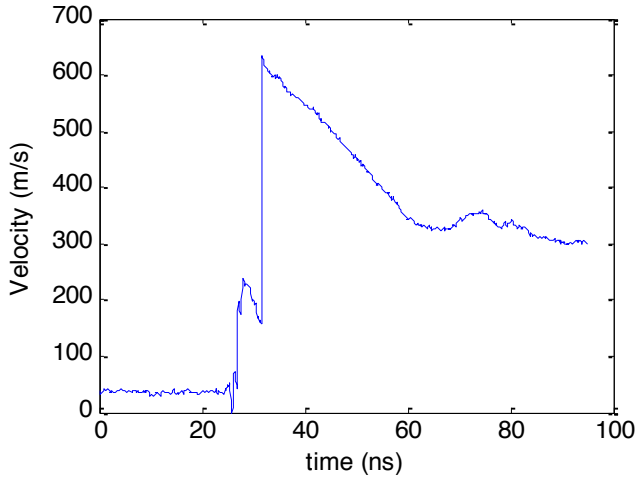

Figure 5: Velocity profile of sample 25513

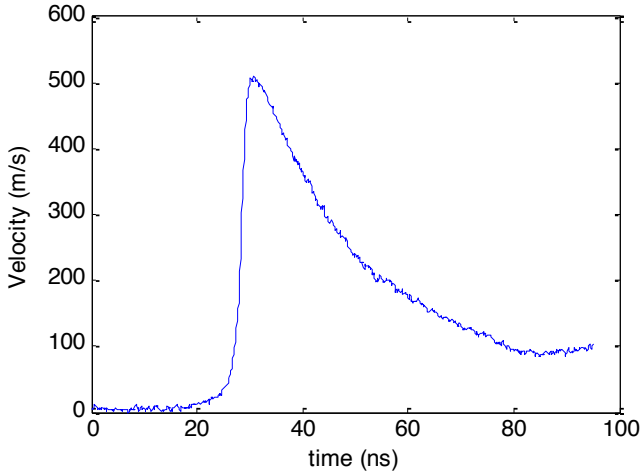

Figure 6: Velocity profile of 25514

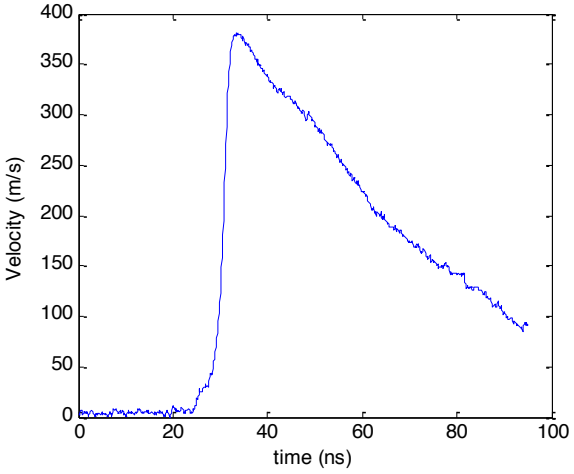

Figure 7: Velocity profile of sample 25510

From the velocimetry data, maximum pressure (σ_{Max}) and spall strength (σ_{spall}) were calculated using the following equations:

$$P_{max}^{Target} = \frac{u_p^T}{u_p^{VISAR}} \rho^{Cu} u_{peak}^{VISAR} U_s^{Cu}$$

$$\sigma_{spall} = \frac{1}{2}\rho^{Cu} U_s^{Cu} u_{max}^{VISAR} - \frac{1}{2}\rho^{Cu} U_s^{Cu} u_{min}^{VISAR}$$

where $\frac{u_p^T}{u_p^{VISAR}}$ was taken to be $\frac{1}{2}$ due to symmetric impact. Density of copper, ρ^{Cu}, was taken to be 8.930 Mg/m^3. The shock velocity, U_s^{Cu}, was calculated using the EOS for Copper:

$$U_s^{Cu} = C_0 + s^{Cu} u_p$$

C_0 = 3.94 km/s, s^{Cu} = 1.49, and u_p, u_{max}^{VISAR}, and u_{min}^{VISAR} were taken from the VISAR record [6]. Table 1 outlines the testing conditions, pressure, and spall strength for each sample.

Table 1: Testing conditions for each sample

Shot Number/ microstructure	Laser Energy (J)	Pulse (ns)	σ_{Max} (GPa)	σ_{spall} (GPa)
25510/intact	48.3	20	7.69	n/a
25513/split	n/a	20	13.5	5.1
25514/partially split	81.5	20	10.5	n/a

Spall strength for 25510 and 25514 was unable to be calculated, since there was no clear indication of a minimum particle velocity, i.e., a spall pullback. Damage was localized mostly on the boundary, as will be shown later, which makes detecting it more difficult using velocimetry.

The raw line-VISAR and TIDI records for all the samples are shown in Figures 8 through 10. The shock front in each of the samples is rippled due to the surface perturbations on the ablated sides, shown in the line-VISAR images. TIDI records for all samples are at the later timing, which was taken 6.5 ns later than the initial. Figures 8 and 9 show some of the fringes below the initial ripple to be shifting horizontally. The shifts on the line-VISAR profile are also observed in the TIDI profile as warping. The line-VISAR and TIDI plots for 25510, or the intact boundary, are shown in Figure 10. As these features mentioned above for 25513 and 25514 are not visible for 25510, they can be attributed to splitting of the boundary. Note that towards the middle of the VISAR record in Fig. 8a, it is possible to see a pullback signal in the center fringe, which is likely to correspond to the grain boundary.

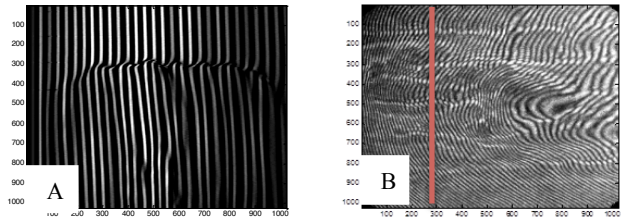

Figure 8: a) Line-VISAR of 25513, b) TIDI of 25513

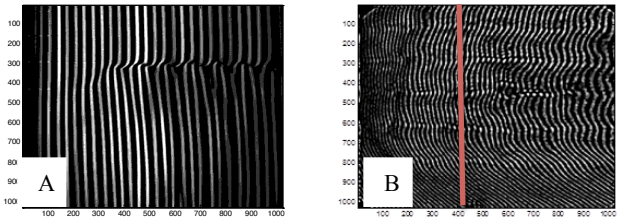

Figure 9: a) Line-VISAR of 25514, b) TIDI of 25514

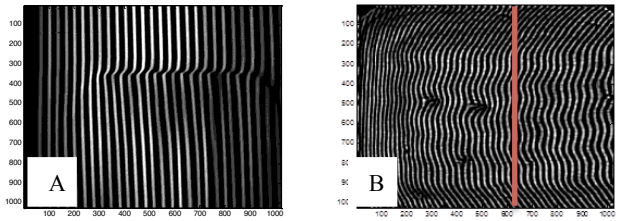

Figure 10: a) Line-VISAR of 25510, b) TIDI of 25510

Line traces of out-of-plane displacement obtained from the TIDI measurements on the back (diagnostic surface) of each sample are shown in Figures 11 – 13. The red line on the TIDI images corresponds to the column that was used as the line trace. The amplitude of the imprinted perturbation on the backside of the sample and its evolution provides information on material behavior and how the grain boundary might affect it. The large displacement seen in the center of the sample on Figure 12 could be caused by the boundary splitting. Table 2 gives the perturbation amplitudes measured for each sample.

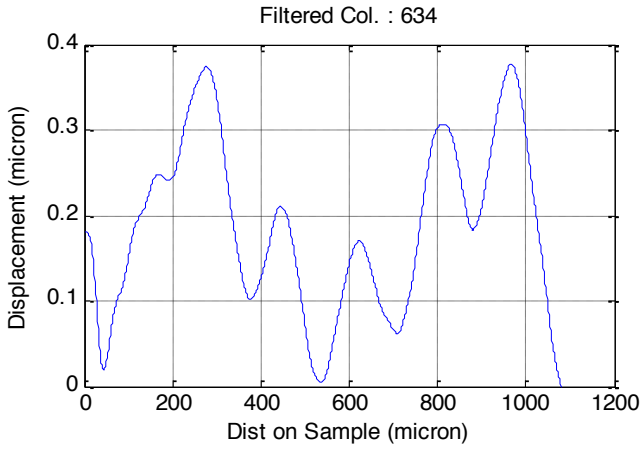

Figure 11: TIDI of 25510

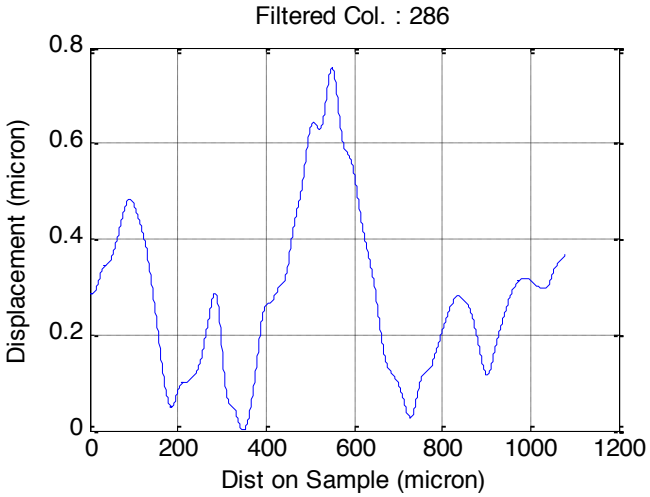

Figure 12: TIDI of 25513

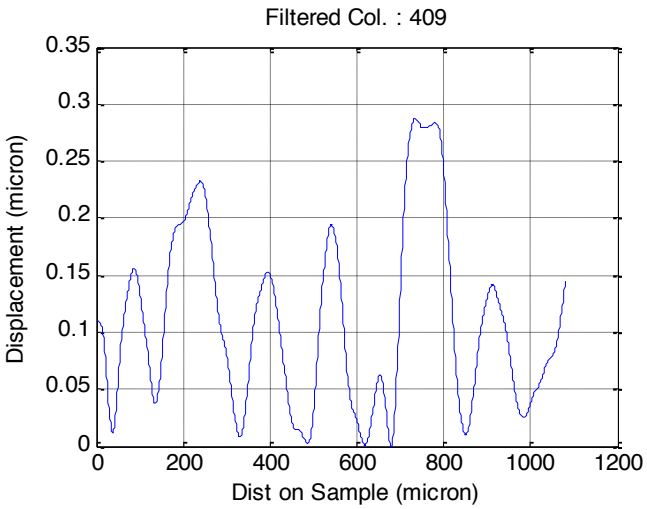

Figure 13: TIDI of 25514

Table 2: Free Surface Amplitudes from TIDI

Shot Number	Average Free Surface Amplitude (microns)
25510	0.173
25513	0.37
25514	0.147

Sections of all three samples, shown in Figures 14 – 16, display either damage nucleation at the boundary or a broken boundary where all voids nucleated and coalesced together, making the boundary a weak link. In the sections for 25510, more damage was seen in the [001] grain. Shallow voids did appear in subsequent sections within the grains. The voids in each of the samples appeared to oscillate slightly within the grain, which can be attributed to the rippled surface. Grain orientations for Figures 14 – 16 are presented in the shock direction.

Figure 14: Sample section of 25510.

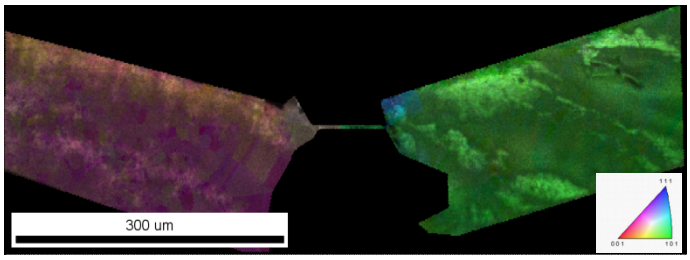

Figure 15: Sample section of 25513

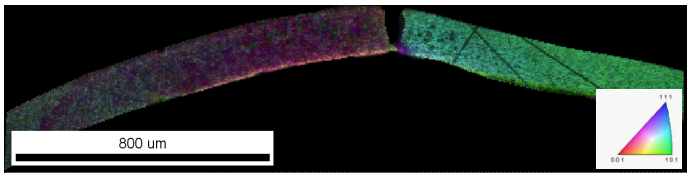

Figure 16: Sample section of 25514

CONCLUSIONS

Experiments were performed in bicrystalline copper with varying testing conditions led to intact, partially unzipped, and unzipped boundaries. In each of the samples it was found that voids nucleated at the boundary, causing incipient, intermediate, and full spallation of the sample and making the boundary a weak point. Splitting of the boundary occurs at particle velocities at or above 500 m/s and can be observed in the line-VISAR and TIDI images.

ACKNOWLEDGMENTS

This work was funded by the Department of Energy, NNSA, under SSAA Grants # DE-FG52- 06NA26169, DE-FG52-10NA29653 and DE-NA0002005 and DE-SC0008683

from the Office of Fusion Energy Science. Access to the TRIDENT Facility, the use of facilities within the LeRoy Eyring Center for Solid State Science at ASU, as well as the use of facilities within the ASU Center for Solid State Electronics Research (CSSER) is gratefully acknowledged.

REFERENCES

[1] Meyers, M. A., 1994. *Dynamic Behavior of Materials*. John Wiley & Sons, New York.
[2] Brown, A, 2014. "3-D Characterization of Microstructural Weak Links for Spall Damage in Shock Loaded Copper Multi- and Polycrystals." Thesis. Arizona State University, School for Engineering Matter, Transport, and Energy, Tempe.
[3] Bingert, J. F., Henrie, B. L., and Worthington, D. L., 2007. "Three-Dimensional Characterization of Incipiently Spalled Tantalum." Metallurgical and Materials Transactions A., 38A: p,1712-1721.
[4] Wayne, L., Krishnan, K., DiGiacomo, S., Kovvali, N., Peralta, P., Luo, S.N., Greenfield, S., Byler, D., Paisley, D., McClellan, K.J., Koskelo, A., Dickerson, R., 2010. "Statistics of weak grain boundaries for spall damage in polycrystalline copper." Scripta Materialia, 63: p.1065-1068.
[5] Brown, A., Wayne, L., Pham, Q., Krishnan, K., Peralta, P., Luo, S.N., Patterson, B. M., Greenfield, S., Byler, D., McClellan, K.J., Koskelo, A., Dickerson, R., Xiao, X, 2014. "Microstructural Effects on Damage Nucleation in Shock-Loaded Polycrystalline Copper." Metallurgical and Materials Transactions A.
[6] Peralta, P., DiGiacomo, S., Hashemian, S., Luo, S. N., Paisley, D., Dickerson R., Loomis, E., Byler, D., McClellan, K. J., D'Armas, H., 2008. "Characterization of Incipient Spall Damage in Shocked Copper Multicrystals." International Journal of Damage Mechanics, 18, p.393-413.
[7] Livescu, V., Bingers, J.F., Mason, T.A., 2012. "Deformation twinning in explosively-driven tantalum." Materials Science & Engineering A, 556, p. 155-163.
[8] Wayne, L., 2009. "Three-Dimensional Characterization of Spall Damage at Microstructural Weak Links in Shock-Loaded Copper Poylcrystals." Arizona State University, School for Engineering Matter, Transport, and Energy, Tempe.
[9] Brown, A., Krishnan, K., Wayne, L., Peralta, P., Luo, S.N., Byler, D., Patterson, B., 2013. "3-D Characterization of Global and Local Microstructural Effects on Spall Damage in Shock Loaded FCC Metals: Experimental and Modeling." ASME IMECE, San Diego, CA, P. 65642.
[10] Perez-Bergquist, A.G., Cerreta, E.K., Trujillo, C.P., Cao, F., Gray III, G.T., 2011 "Orientation dependence of void formation and substructure deformation in a spalled copper bicrystal." Scripta Materialia, 65, p. 1069-1072.
[11] Barker, L. M., Hollenbach, R. E., 1972. "Laser interferometer for measuring high velocities of any reflecting surface." Journal of Applied Physics, 43, 4669-4675.
[12] Greenfield, S. R., Luo, S. N., Paisley, D. L., Loomis, E. N., Swift, D. C., Koskelo, A. C., 2007. "Transient Imaging Displacement Interferometry Applied to Shock Loading." AIP Conference Proceedings, Shock Compression of Condensed Matter, 955, p. 1093-1096.
[13] Lou, S.N., Peralta, P., Ma, C., Paisley, D., Greenfield, S., Loomis, E., 2007. "Sapphire (0 0 0 1) surface modifications induced by long-pulse 1054nm laser irradiation." Applied Surface Science, 253, pp. 9457-9466.
[14] Kanel, G. I., Rasorenov, S. V., Fortov, V. E, 1992. "Shock-wave and High-strain-rate Phenomena in Materials." Ed.M. A. Meyers, L. E. Murr, K. P. Staudhammer. Marcel Dekker, New York, p. 775.
[15] Minich, R. W., Cazamias, J. U., Kumar, M., Schwartz, A. J., 2004 "Effect of microstructural length scales on spall behavior of copper." Metallurgical and Materials Transactions A, 35.9, 2663-2673. Web.